Aerodynamic Performance and Static Stability Characteristics of Aircraft with Tail-Mounted Propellers

van Arnhem, N.; de Vries, R.; Sinnige, T.; Vos, Roelof; Veldhuis, L.L.M.

DOI
10.2514/1.C036338

Publication date
2021

Document Version
Final published version

Published in
Journal of Aircraft: devoted to aeronautical science and technology

Citation (APA)
van Arnhem, N., de Vries, R., Sinnige, T., Vos, R., & Veldhuis, L. L. M. (2021). Aerodynamic Performance and Static Stability Characteristics of Aircraft with Tail-Mounted Propellers. *Journal of Aircraft: devoted to aeronautical science and technology*, *59*(2), 415-432. https://doi.org/10.2514/1.C036338

JOURNAL OF AIRCRAFT
Vol. 59, No. 2, March–April 2022

Aerodynamic Performance and Static Stability Characteristics of Aircraft with Tail-Mounted Propellers

Nando van Arnhem,* Reynard de Vries,† Tomas Sinnige,‡ Roelof Vos,§ and Leo L. M. Veldhuis¶
Delft University of Technology, 2629 HS Delft, The Netherlands

https://doi.org/10.2514/1.C036338

In this combined experimental and numerical study, the propeller–airframe aerodynamic interaction is characterized for an aircraft configuration with propellers mounted to the horizontal tailplane. The contributions of the propeller and airframe to the overall loading are distinguished in the experimental analyses by using a combination of external balance and internal load cell data. Validated computational fluid dynamics simulations are then employed to quantify the interaction at a component level. The results show that the propeller installation shifts the neutral point aft with increasing propeller thrust. For the configuration considered herein, the yawing moment due to sideslip is increased by approximately 10%, independent of the propeller thrust coefficient. The changes in propeller loading due to the airframe-induced flowfield are the dominant factor to change the airframe stability and performance. The prominent installation effects occur at high angle of attack, because in that condition the propeller experiences a significant nonuniform inflow that affects the propeller and tailplane. The relatively large propeller diameter compared with tailplane span leads to a change of the tailplane root vortex that causes the tailplane effectiveness to reduce with an inboard-up rotating propeller.

Nomenclature

b	=	span, m
C_D	=	drag coefficient, $D/q_\infty S_w$
C_L	=	lift coefficient, $L/q_\infty S_w$
C_m	=	pitching-moment coefficient, $m/q_\infty S_w \bar{c}$
C_n	=	yawing-moment coefficient, $n/q_\infty S_w \bar{c}$
C_{N_p}	=	propeller normal-force coefficient, $N_p/\rho_\infty n^2 D_p^4$
C_{p_s}	=	static-pressure coefficient, $p - p_\infty/q_\infty$
C_{p_t}	=	total-pressure coefficient, $(p_t - p_{t_\infty}/q_\infty) + 1$
C_Q	=	torque coefficient $Q/\rho_\infty n^2 D_p^5$
C_T	=	thrust coefficient, $T/\rho_\infty n^2 D_p^4$
C_X	=	axial-force coefficient, $F_x/q_\infty S_w$
C_{Y_p}	=	propeller side-force coefficient, $F_{Y_p}/\rho_\infty n^2 D_p^4$
$c, \bar{c}$	=	chord, mean aerodynamic chord, m
c_d	=	section drag coefficient, $d/q_\infty c$
c_n	=	section normal-force coefficient, $n/q_\infty c$
D	=	diameter, m; drag, N
d	=	section drag, N · m^{-1}
F	=	force, N
J	=	advance ratio, V_∞/nD_p
L	=	lift force, N; length, m
l	=	length of a moment arm, m
M	=	Mach number
m	=	pitching moment, N · m
N	=	normal force, N
n	=	propeller rotational speed, s^{-1}; yawing moment, N · m; section normal force, N · m^{-1}
P_s	=	shaft power, W
p	=	pressure, Pa
Q	=	torque, N · m
Q_C	=	torque coefficient, $Q/q_\infty S_p D_p$
q	=	dynamic pressure, Pa
R	=	radius, m
Re_c	=	Reynolds number based on chord
r	=	radial coordinate, m
S	=	area, m^2
T	=	thrust (along propeller rotation axis), N
T_C	=	thrust coefficient, $T/q_\infty S_p$
$T_{C,x}$	=	thrust coefficient along x axis, $F_{x_p}/q_\infty S_p$
u, v, w	=	velocity in Cartesian system, m · s^{-1}
V	=	velocity, m · s^{-1}
X, Y, Z	=	propeller coordinate system, m
x, y, z	=	aircraft coordinate system, m
y^+	=	dimensionless wall distance
$\mathcal{AR}$	=	aspect ratio
α	=	angle of attack, deg
β	=	angle of sideslip, deg
Γ	=	circulation, m^2 · s^{-1}
δ	=	deflection, deg
ε	=	downwash angle, deg
η_p	=	propeller efficiency, TV_∞/P_s
η_x	=	propeller efficiency in x direction, $F_{x_p} V_\infty/P_s$
ρ	=	density, kg · m^{-3}
σ	=	sidewash angle, deg
ϕ	=	propeller phase angle, deg
ω	=	vorticity, s^{-1}
$\tilde{\omega}$	=	normalized vorticity, $\omega\bar{c}/V_\infty$
ω^*	=	normalized vorticity, $\omega D_p/V_{eff}$

Subscripts

a	=	axial component
af	=	airframe
eff	=	effective
f	=	flap
ht	=	horizontal tail
ins	=	installed
max	=	maximum
min	=	minimum

Presented as Paper 2019-3036 at the AIAA Aviation 2019 Forum, Dallas, TX, June 17–21, 2019; received 27 December 2020; revision received 12 August 2021; accepted for publication 15 August 2021; published online 12 November 2021.

*Ph.D. Candidate, Flight Performance and Propulsion Section, Faculty of Aerospace Engineering; n.vanarnhem@tudelft.nl. Member AIAA.
†Ph.D. Candidate, Flight Performance and Propulsion Section, Faculty of Aerospace Engineering. Member AIAA.
‡Assistant Professor, Flight Performance and Propulsion Section, Faculty of Aerospace Engineering. Member AIAA.
§Assistant Professor, Flight Performance and Propulsion Section, Faculty of Aerospace Engineering. Associate Fellow AIAA.
¶Full Professor, Flight Performance and Propulsion Section, Faculty of Aerospace Engineering. Member AIAA.

p = propeller
s = static
t = tangential component, total
vt = vertical tail
w = wing
∞ = freestream

Superscript

′ = local quantity

I. Introduction

MODERN propellers are an attractive means of aircraft propulsion for short- to medium-range missions because of their inherent high efficiency compared with technology-equivalent turbofans [1–11]. Block fuel savings up to 20% have been anticipated for missions that are climb and approach dominated [4,12–14]. Flights of medium range (1000–2000 nautical miles) with design cruise Mach numbers between 0.7 and 0.8 are predicted to achieve fuel savings of 10–20% [12,14,15]. Despite the lower or equal community noise levels compared with turbofans [12,14], a drawback of unducted propellers is increased cabin noise [16,17], in particular for flight Mach numbers ranging from 0.6 to 0.8. This noise is caused by an airborne contribution due to the unsteady pressure field induced by the rotating blades and the propeller–airframe interaction, and a structureborne contribution due to vibrations from the engines, propellers, and propeller–airframe interaction [18–21]. However, because of the significant propulsive efficiency benefit, as consistently demonstrated in several industrial and governmental research programs, propellers remain appealing for the next generation of energy-efficient aircraft.

Despite successful reductions of cabin noise by employing various techniques [16,17,19,22–29], the cabin noise levels of current turboprops are still several decibels higher compared with turbofan-driven aircraft [17,20,25,30,31]. This noise penalty is aggravated due to the tonal components of the noise spectrum, which are perceived by passengers as more annoying than broadband noise [17]. Historically, large propeller-driven commercial aircraft for passenger transport have been equipped with wing-mounted tractor propellers. For these aircraft, the highest sound pressure levels on the fuselage outer surface fall within ± 30 deg from the propeller rotation plane [17,32,33]. The distribution of the overall sound pressure level inside the cabin is less concentrated because of various transmission mechanisms [30,34], and the highest interior noise level is typically located approximately one diameter downstream of the propeller rotation plane, near the wing–fuselage junction [25,30,34]. Alternatively to the passive shielding methods that have been investigated for these configurations [5,31,35], a larger reduction in perceived airborne and structureborne noise can potentially be achieved by mounting the propeller propulsion system to the tailplane or a pylon, as already proposed in the 1980s [1,4,6,9,21,30,36]. For such a aft-mounted propulsion arrangement, several additional advantages have been identified from an aerodynamic-efficiency perspective, such as the potential of an extended region of laminar flow on the wing [37], and reduced adverse compressibility effects on the wing and nacelle at flight Mach numbers up to 0.8 [38]. Recently, industry has expressed renewed interest in the aft-mounted propeller configuration, e.g., aircraft manufacturer Embraer [39] and aircraft engine manufacturer SAFRAN [8].

The unconventional placement of the propeller propulsion system at the back of the aircraft also brings challenges in terms of design, performance, structural integration, and operation. Compared with the conventional wing-mounted tractor configuration, on which extensive literature has been published, a number of differences in the type and magnitude of propeller–airframe interaction effects can be distinguished for the rear-mounted propellers. In a wing-mounted tractor configuration, the integral propeller forces are only marginally influenced by the wing-induced flowfield [40–42], and the propeller contribution to aircraft stability and trim can be estimated using linearized models [43]. Typically, the propeller forces are treated determined without including the influence of the airframe [44]. In these configurations, the propeller-induced flowfield primarily affects the forces on the wing, which have a limited effect on static stability due to the close proximity to the aircraft center of gravity. On the other hand, the complex flowfield at the tail surfaces leads to large variations of static longitudinal stability between various aircraft attitudes [43,45–49]. Moreover, the wing-induced crossflow to the vertical tailplane affects the directional stability and trim [45,49–52].

From the preliminary design activities on different rear-mounted propeller configurations, the pylon-mounted and horizontal-tail-mounted tractor configurations were found to be most feasible, based on various performance indicators [1,6,30,53]. Recently, the horizontal-tail-mounted configuration was revisited in the European CleanSky research project Innovative turbopROp configuratioN (IRON) [37,54,55]. These studies concluded that, compared with a wing-mounted propeller configuration, the relatively large excursion of the center of gravity requires larger tail surfaces and introduces additional trim drag, also observed in Ref. [56]. These losses may even offset any benefits gained from a partially laminar wing. For example, in Ref. [30] it is estimated that the fuel saving potential of using propellers instead of turbofans could reduce with 50% compared with the wing-mounted propeller configuration for missions of over 1500 nautical miles. These previous studies, however, acknowledge the limited details of the complex propeller–airframe aerodynamic interaction that was included in the performance assessments. For example, to assess the impact on static stability, the rear-mounted propeller was treated as an isolated propeller at a distance from the aircraft center of gravity, neglecting the changes in the airframe and propeller forces due to the aerodynamic interaction. The main wing, high-lift system, and fuselage induce a nonuniform flowfield to the propeller that affects both time-averaged and unsteady propeller forces in the out-of-plane and in-plane directions, as well as the propeller efficiency. As the propeller is relatively far from the aircraft center of gravity, the change in propeller loading due to the nonuniform inflow impacts the aircraft stability and trim characteristics. A variety of studies on propeller–wing aerodynamic interaction have indicated that the wing aerodynamic characteristics are highly influenced by the location and rotation direction of the wing-mounted tractor propeller [42,57–59]. Therefore, the close proximity of the propeller to the stabilizing surfaces further affects the stabilizing contribution of the tailplane.

Despite the various works published on propeller–airframe aerodynamic interaction for several decades of which Ref. [2] has provided an overview of a range of studies, a synthesis of the aerodynamic interaction between rear-mounted propellers and the airframe has only been addressed by a few authors. Earlier experimental work and conceptual design studies [1,30,60–62] on the rear-mounted propeller configuration showed that the overall longitudinal and lateral static stability are not adversely affected by the propeller installation, which is attributed to a more effective horizontal tailplane and the stabilizing contribution of the propeller normal force [63]. The most detailed experimental campaign performed on such configuration is presented by Ridder [62]. In that study, integral force measurements show an appreciable effect of the propeller installation on the change in trim, static stability, and control authority. The measured flowfields also confirm a nonuniform inflow to the propeller. However, the relative contributions of the propeller and airframe to the overall vehicle performance were not assessed, while these are key in order to understand the relevant interaction phenomena. Therefore, a more detailed breakdown of the propeller–airframe interaction in this unconventional configuration is required, as this can lead to improved performance predictions and, ultimately, improved design choices.

The goal of this paper is therefore to characterize the changes in aircraft static stability, control, and performance due to the rear-mounted propellers by analyzing the time-averaged propeller–airframe aerodynamic interactions. To this end, analyses were performed on a 5%-scale model of a low-wing regional turboprop aircraft configuration with tail-mounted propellers. A combined experimental and numerical approach was selected to analyze the aerodynamic interaction on both component and aircraft level for a large range of operating conditions. The experimental setup is used to assess the time-averaged effect of the propeller installation on the propellers and at aircraft level. The numerical setup complements the

experimental results for a limited number of cases to obtain the load distributions on the tailplane and propellers, which provide further insight into the dominant interaction phenomena.

II. Experimental Setup

A. Wind-Tunnel Facility and Model

The experimental campaign was performed at the Low-Turbulence Tunnel (LTT) at Delft University of Technology, a closed-return low-speed wind tunnel. The measurements were performed at a free-stream velocity of 40.00 ± 0.02 m/s ($Re_{\bar{c}} = 4.54 \cdot 10^5, M = 0.12$). At these conditions, the turbulence level is below 0.03% [64]. The aircraft model was suspended by a three-point support system, shown in Fig. 1, in an octagonal test section, with dimensions as indicated in Fig. 2. The wind-tunnel walls are tapered to mitigate blockage and avoid buoyancy drag from the boundary layer that forms on these walls. The conceptual aircraft model represents a regional aircraft with a cruise Mach number between 0.6 and 0.7 for 130 passengers, comparable to the IRON configuration [55], which is referred to as the "full-scale aircraft." This geometry, of which an overview is provided in Table 1 and Fig. 2, was designed based on Refs. [1,30,37,60]. The wing had zero quarter-chord sweep, a taper ratio of 0.40, and an aspect ratio of 8.46. This aspect ratio of the model is relatively low compared with existing and envisioned turboprop aircraft, with aspect ratios ranging between $\mathcal{AR} = 8$ and $\mathcal{AR} = 14$ [1,9,65–69]. The implication is that the downwash gradient of the aircraft model is relatively high. The encounter between the propeller and wing wake would initiate at a slightly lower angle of attack if the aircraft had a more slender wing.

High-lift conditions were simulated by attaching Junkers flaps to the main wing. The configuration without the flaps installed is referred to as the "clean configuration." The nacelles were aligned with the fuselage centerline and were mounted at 69% of the horizontal-tail semispan. Both inboard and outboard parts of the horizontal tail were equipped with elevators with a chord ratio of 25%. The distance between the propeller rotation plane and the leading edge of the tailplane was selected as $1.2R_p$, based on suggestions in Ref. [70]. The CAD geometries of the model and wind tunnel section and the coordinates of the wing DU 96-150 airfoil are attached to this paper as Supplemental Materials S1.

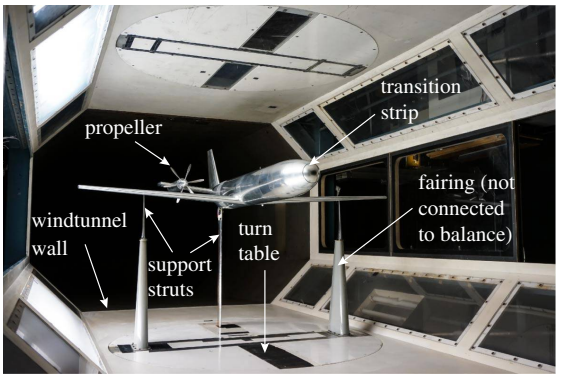

Fig. 1 Experimental setup of the horizontal-tail-mounted propeller configuration installed in the Low Turbulence Tunnel at Delft University of Technology.

The wind-tunnel model was equipped with two six-bladed, steel propellers, which had been employed and characterized in previous studies [71–73]. The corresponding performance and flowfield data of the isolated propeller that serve as reference throughout the current paper are described in Ref. [71]. The blade pitch of 45 ± 0.05 deg at 70% radius and the advance ratios were selected such that the range of nondimensional force coefficients (C_T, C_P, T_C, Q_C, C_{N_α}) and tip vortex pitches obtained in the experiment are comparable to those of full-scale propellers operating at cruise to climb conditions [28,30,41,63]. The advance ratio was varied between $J = 2.3$ and $J = 1.6$ by changing the rotational speed to achieve thrust coefficients from $T_C = 0.01$, representing approach conditions, up to $T_C = 0.28$, typical for cruise and climb conditions. Both inboard-up (IU), outboard-up (OU), and corotating (CO) propeller configurations were tested to quantify the effect of rotation direction. The propellers were driven by two Lehner 2260/40 electric motors, controlled by a dedicated control program developed in-house, and the rotational speed was registered by means of an optical rotary encoder. The time-averaged rotational speed could be controlled with an accuracy of 0.01 Hz, with maximum fluctuations around the setpoint up to 0.1 Hz. For the propeller-off conditions, which serve as the reference, the propellers were replaced by nonrotating dummy spinners.

To avoid laminar separation and to facilitate a fair comparison with the fully turbulent numerical simulations, the boundary layers were tripped with 2.5-mm-wide transition strips with carborundum particles with an average size of 150 μm on the fuselage, wing, nacelle, and tail surfaces. On the tail surfaces and wing pressure side, the strips were applied at 10% of the chord, whereas on the wing suction side a strip was applied at 5% chord. Transition was verified by means of a microphone for the considered range of operating conditions. The model was manufactured with a surface roughness of less than 0.4 μm and surface irregularities (e.g., countersunk holes) were filled with plasticine.

B. Measurement Techniques and Uncertainty

1. *Integral Force Measurements*

The integral forces on the aircraft model were measured by connecting the supports (Fig. 1) to a six-component external balance that allows for variation of both angle of attack and sideslip. For the considered range in aerodynamic forces, the balance readings had an uncertainty up to 0.02 N, depending on the force component. Two times these values are included in the error bars of the respective force measurements. These error bars also include the spread in data of repeated measurements due to, e.g., aerodynamic hysteresis, variations in operating conditions, or other random errors. The error bars also include the contributions of the uncertainty in the blade-pitch angle (determined in Ref. [71]) and the uncertainty of the rotational speed. Tare measurements were taken to account for the aerodynamic forces of the support struts using measurements of only the support struts (with the model removed). An acquisition time of 20 s was selected to average the measured forces at an acquisition frequency of

Table 1 Main dimensions of the aerodynamic surfaces

Dimension	Wing without flap	Flaps	Horizontal tail	Vertical tail
Area	$S_w = 0.2163$ m^2	$\frac{2S_f}{S_w} = 0.19$	$\frac{S_{ht}}{S_w} = 0.40$	$\frac{S_{vt}}{S_w} = 0.18$
Airfoil	DU 96-150	DU 96-150	NACA 64_2 A015	NACA 0015
Root/tip incidence angle	0 deg / −2 deg	—/0 deg	0 deg /0 deg	0 deg /0 deg
Aspect ratio	8.46	6.10	2.85	1.50
Taper ratio	0.40	1.00	1.00	0.41
Volume coefficient	— —	— —	$\frac{S_{ht}l_{ht}}{S_w\bar{c}} = 1.14$	$\frac{S_{vt}l_{vt}}{S_w b_w} = 0.54$
Control surface area	— —	— —	$0.17S_{ht}$	$0.28S_{vt}$

The vertical tail is defined up to the curved fuselage centerline.

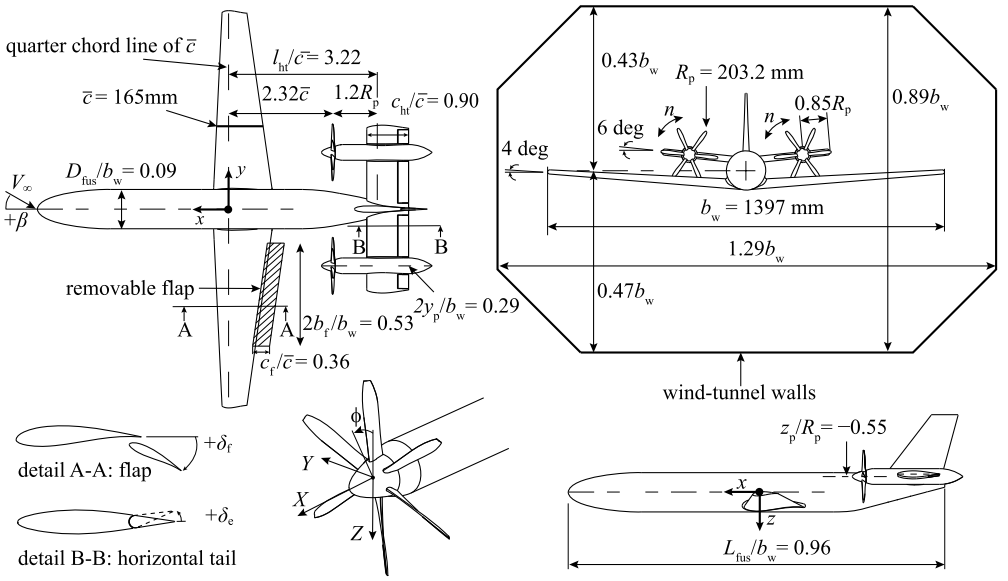

Fig. 2 Technical drawing of the aircraft model and wind tunnel test section.

10 Hz. This resulted in converged mean force estimates at all operating conditions considered.

Because the focus of the study is on the aerodynamic phenomena, and not on the quantification of the absolute aerodynamic coefficients, the experimental data are not corrected for wall effects. To maintain agreement between the computational fluid dynamics (CFD) simulations (with simulated wind tunnel walls) and experiment, all presented results are therefore based on uncorrected data. Classical wall corrections based on lift and drag do not suffice, as is indicated by the wind-tunnel wall pressures presented in Supplemental Materials S2. The propellers cause the wall pressure to vary along the x direction, such that in particular the aircraft pitching-moment coefficient is expected to be slightly influenced by the presence of the walls.

2. Propeller Force Measurements

The propeller forces were measured separately by mounting each electric motor to a six-component strain-gauge load cell, as depicted in Fig. 3. Despite the thermal insulation layer between the electric motor and load cell, the internal temperature of the load cell rose during operation, and it is known that such temperature drifts affect the output of strain-gauge balances [74,75]. A calibration campaign of the installed setup was performed to determine linear temperature compensation coefficients for each force component by using the average readings of two thermocouples mounted close to the load cell that registered the temperature during operation. The uncertainty of the presented propeller force coefficients is the spread in the data of the repeated measurements. No tare measurements were taken of the spinner without blades. Instead, the forces on the spinner of the propeller-off configuration were estimated using the CFD simulations and subtracted from the load cell measurements in order to quantify the forces on the blades and the change in forces on the spinner relative to the propeller-off condition.

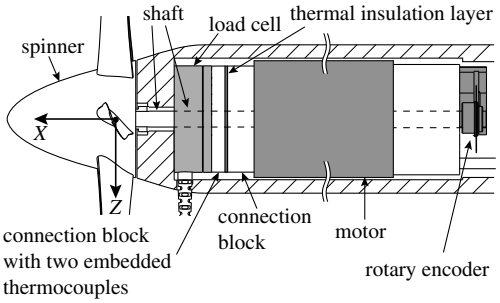

Fig. 3 Schematic of the electric motor and load cell assembly inside the nacelle.

3. Flowfield Measurements

To illustrate the propeller–airframe interaction for a range of conditions as well as for validation purposes, the total pressure was measured by traversing a rake with 74 probes in a plane perpendicular to the freestream at two propeller diameters behind the propeller rotation plane. The measurements were taken in a rectangular grid with resolution of 3 mm in vertical and lateral directions. Maximum instantaneous swirl angles up to 15 deg have been measured [71] in the vortex cores for the conditions presented in this paper. For the internally conical shaped tip of the probes, the associated error of this skewed flow-angle with respect to the probe is less than 1% [76]. The pressures were acquired for 5 s of acquisition time by electronic pressure scanners. The uncertainty of ± 2 Pa (0.2% of q_∞) on the time-averaged values is indicated by the error bars in the graphs of Sec. III. For the force measurements, the wake rake was not installed to avoid its upstream effect on the model.

III. Computational Strategy

A. Computational Setup

The propeller–airframe aerodynamic interactions at a component level were quantified by numerical simulations. These allow for the analyses of the load distributions on the propeller and tailplane surfaces, which could not be measured with the experimental setup. To this end, a half-model excluding support struts and flaps, shown in Fig. 4, was simulated by solving the Reynolds-averaged Navier–Stokes (RANS) equations for compressible flow. The geometry contained the gaps around the elevators, whereas the gap between the spinner and nacelle and the gaps associated with the rudder were sealed for simplicity. The model was placed in a domain with parallel outer boundaries on which a free-slip boundary condition was specified (as sketched in Fig. 2), to resemble the wind-tunnel walls that are diverging by approximately 0.5 deg to compensate for buoyancy effects. On all airframe components a smooth wall with no roughness was assumed. A pressure inlet boundary condition was placed far upstream of the model at $x/b_w = 2.7$. The flow direction is enforced to be normal to this boundary, and the magnitude matches the conditions of the experiment. The domain size is chosen based on the gradients $d\alpha/dx$ and dC_{p_s}/dx. Already at $x/b_w = 2.0$ these gradients have reached negligible values (see Supplemental Materials S2), whereas the boundary is placed further upstream. The total pressure inlet condition ensures that the static pressure (far) upstream the model is not enforced to match the ambient

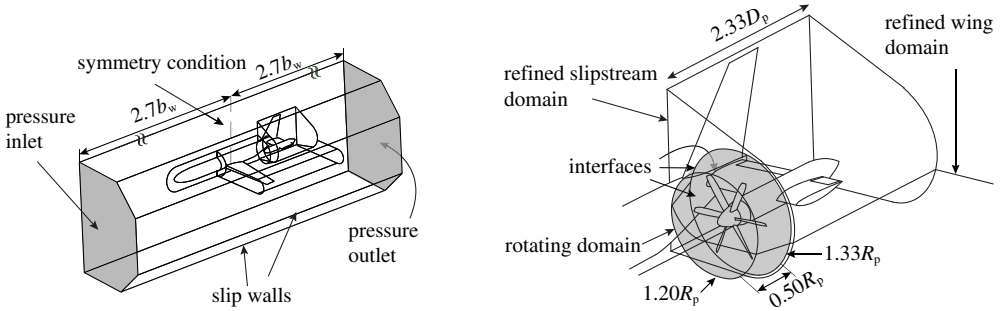

a) Computational domain with boundary conditions. Length of domain not to scale with model **b) Detailed view of the rotating domain containing the propeller**

Fig. 4 Overview of computational domain and boundary conditions.

condition. Far downstream of the model, the average pressure was specified to be equal to ambient conditions. To simulate either an inboard-up or outboard-up propeller rotation direction, a symmetry condition was specified on the symmetry plane of the aircraft. Therefore, only the counter-rotating propeller configurations could be simulated, in contrary to the experimental setup, which also allowed for the corotating configuration.

A full-blade approach was selected over lower-order models such as actuator-disk approaches. In Ref. [77] it is shown that even though a relatively accurate representation of the flowfield can be obtained by using an actuator disk model, the propeller load distribution should be known in advance. Moreover, for an aerodynamic surface like the tailplane that is submerged in a highly distorted and time-dependent flowfield, a time-accurate representation is most suitable to accurately determine the time-averaged normal force on this aerodynamic surface, as demonstrated in Ref. [77]. The most accurate representation of the full-blade is therefore deemed required to achieve the objectives of this paper.

The unstructured volume grid contained tetrahedral elements with refined grids in the proximity of the model, indicated in Fig. 4. The propeller was placed in a rotating domain, indicated in Fig. 4b, using the sliding mesh approach [78] by defining interfaces on each side. The cyclic symmetric propeller grid was equal to the one used in Ref. [71], which presents an extensive validation. The cell size ($0.032R_p^3$) of the domain adjacent to the rotating domain containing the horizontal tail was based on the same reference. Wall refinements were applied and an inflation layer of 25 layers with a growth rate of 1.20 was constructed on all no-slip walls. The first-layer thickness on each component was selected to comply with a $y^+ \leq 1$. On the wing and propeller a mapped surface mesh was constructed. The selected grid including propeller contained 60.5 million cells, whereas the grid of the propeller-off condition contained 51.8 million cells. The reader is referred to Ref. [71] for the discretization error of the grid for the propeller forces and slipstream quantities. No dedicated grid refinement study on aircraft level was performed. Instead, the results on the current grid are put in perspective in the validation study presented in the next section.

ANSYS® Fluent Release 18.1 [78], a commercial, unstructured, finite-volume, cell-centered solver was used. A second-order upwind spatial discretization was employed, using a coupled pressure–velocity scheme. The Spalart–Allmaras turbulence model with the strain/vorticity-based production equation was applied to close the system of equations. The inlet eddy–viscosity ratio of 0.21044 was based on recommendations by Spalart and Rumsey [79]. Standard sea-level atmospheric conditions were used for the freestream flow, which was assumed an ideal gas. Sutherland's law was applied to predict the corresponding dynamic viscosity. The simulations without propeller were solved using the steady RANS equations, whereas the full-blade simulations were solved in a time-accurate manner, with a time step equivalent to 2 deg propeller rotation with 35 inner iterations, using a second-order temporal discretization. As the comparisons between propeller-on and propeller-off are at low angle of attack, the difference is not expected to influence the results.

B. Validation of Computational Setup

The numerical setup is validated by comparing to the experimental results. Only the validation of the full aircraft is described in the current paper. The reader is referred to Ref. [71] for the validation study of the isolated propeller.

In Fig. 5a the computed integral lift and drag are compared with the experimental data. At low angles of attack, the primary aspect of interest is performance, as this is the cruise condition. At high angles of attack, where the flowfield at the tailplane is highly distorted due to separated flow from the wing, stability aspects are of interest. In the linear part of the lift curve ($\alpha \leq 5$ deg), the computed lift coefficients coincide with the experimental curve. The initiation of trailing-edge separation from $\alpha > 5$ deg is consistent with observations of the wall-shear lines visualized using fluorescent oil-flow (provided as Supplemental Materials S3). These oil-flow images also indicate that

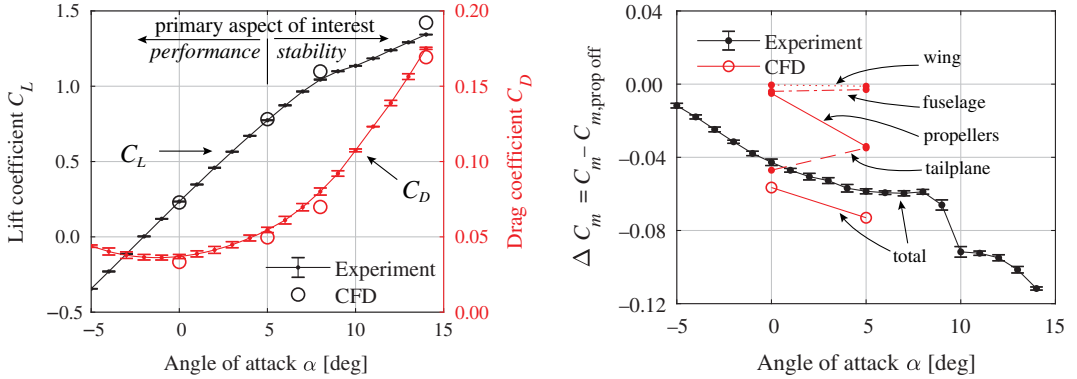

a) Comparison of lift and drag, propeller off. Highlighted regions of interest indicate the associated focus of the study **b) Comparison of the change in pitching moment for the inboard-up rotation direction**

Fig. 5 Comparison of aircraft performance data from CFD and experiment.

at $\alpha = 10$ deg a large region of the wing–fuselage junction experienced reversed flow, in line with the local reduction lift between $y/b_w < 0.4$, shown in the lift distributions provided as Supplemental Materials S4. The lift is overpredicted by 6% by CFD at $\alpha = 14$ deg, attributed to the complex flow structures at the wing–fuselage junction and the sensitivity of the CFD solution to the choice of turbulence model. The results at these conditions will therefore be used to explain the aerodynamic interactions instead of quantifying changes in performance. The drag curve shows that there is a clear offset of approximately 50 drag counts with the experimental data, partially caused by the added drag of the aerodynamic interaction of the supports with the model [80] (which remains after subtracting the tares), the use of a relatively thick transition strip in the experiment that was not modeled in the simulations, and the finite roughness of the wind-tunnel model (contrary to the assumed hydraulically smooth wall in the CFD simulations).

Because the quantification of the stability derivatives is an important aspect of the current paper, the computed change in the pitching-moment coefficient due to the propeller installation is compared with the experimental data in Fig. 5b. The breakdown of the CFD results reveals that the propellers have negligible effect on the fuselage and wing forces. The propellers are a stabilizing contribution, whereas the tailplane contribution to stability reduces due to propeller installation. The gradient over the interval $\alpha = [0, 5]$ deg from the CFD is $\Delta C_{m,\alpha} = -3.24 \cdot 10^{-3}$ deg^{-1}, whereas in the experiment the gradient is $\Delta C_{m,\alpha} = -3.17 \pm 0.03 \cdot 10^{-3}$ deg^{-1}. These values indicate that the change in stability is captured with sufficient agreement to formulate qualitative and quantitative conclusions based on these simulations.

The change in axial force relative to the drag of the isolated airframe, $\Delta C_X = C_{X,\text{prop-on}} - C_{X,\text{prop-off}}$, is a quantitative measure of the propeller–airframe aerodynamic interaction and it is not dependent on the underprediction of $C_{D_{\min}}$. Table 2 shows that the predicted change of C_X nearly falls within the experimental uncertainty, especially at $\alpha = 0$ deg. These values indicate that the CFD model is suitable to quantify the effect of the propeller installation on overall aircraft performance.

Simulations of the flow phenomena of the propeller–airframe interaction are validated by comparing the total-pressure field at the same location as the measured flowfield. The magnitude of the total pressure represents viscous losses and the added momentum by the propeller, whereas the shape of the total-pressure field is determined by the in-plane induced velocity field and therefore encompasses the aerodynamic interaction. Figure 6 compares the measured total-pressure fields with time-averaged full-blade CFD results. Only for the corotating case experimental data are available, while only the inboard-up and outboard-up cases are simulated. The simulated outboard-up case is therefore mirrored in the xz plane for comparison purposes. It is noted that the aerodynamic coupling between the port side and starboard side and the small crossflow at the vertical tailplane, discussed in Sec. V.C, are absent in the CFD data. Qualitatively, all flow features observable in the experimental data are also present in the CFD results: the tip vortex from the horizontal tail, the shear of the nacelle wakes, the distinct shapes of the fuselage and wing wakes, the shear of the slipstream, the nonaxisymmetric loading of the propeller, and the interaction of the propeller tip vortex with tailplane tip vortex. The cropped contours on the upper side of the slipstream are an artifact of low measurement resolution in the upper region of the survey plane.

Survey lines b–d show that the location of the wing wake is excellently predicted by the CFD simulations on the inboard side, with an only slight underprediction of the downwash on the outboard sections. This indicates that the combination of local downwash produced by the wing and tailplane is properly captured. The wake thickness in the CFD simulations is slightly underpredicted, in line with the lower $C_{D_{\min}}$ value from the simulations. The nacelle wake (survey line a) shows excellent agreement with experimental results, indicating that the complex interaction between the propeller hub vortex and the viscous nacelle wake is properly captured. The largest deviations appear at the edge of the slipstream, where the experimental flowfield shows a larger contraction and a larger gradient, also reflected by the translation of the wing wake in survey line a. It is known that the large gradients in these shear layers quickly diffuse downstream of the propeller in the numerical simulation (see, e.g., Ref. [77]), despite the fine grid in the slipstream domain. It is concluded that the observed agreement with experiment is sufficient to predict both the integral forces and flowfields and their associated trends that are caused by the propeller–airframe interaction.

Table 2 Change in axial force on the airframe and propeller from the CFD simulations relative to the experimental results

Angle of attack [deg]	0	0	5	5
Rotation direction	Inboard-up	Outboard-up	Inboard-up	Outboard-up
$\frac{\Delta C_{X,\text{CFD}}}{\Delta C_{X,\text{exp}}} - 1$	$+0.6\% \pm 0.5\%$	$+1.1\% \pm 0.6\%$	$-2.5\% \pm 0.7\%$	$-1.8\% \pm 0.7\%$

Indicated uncertainty corresponds to the experimental values.

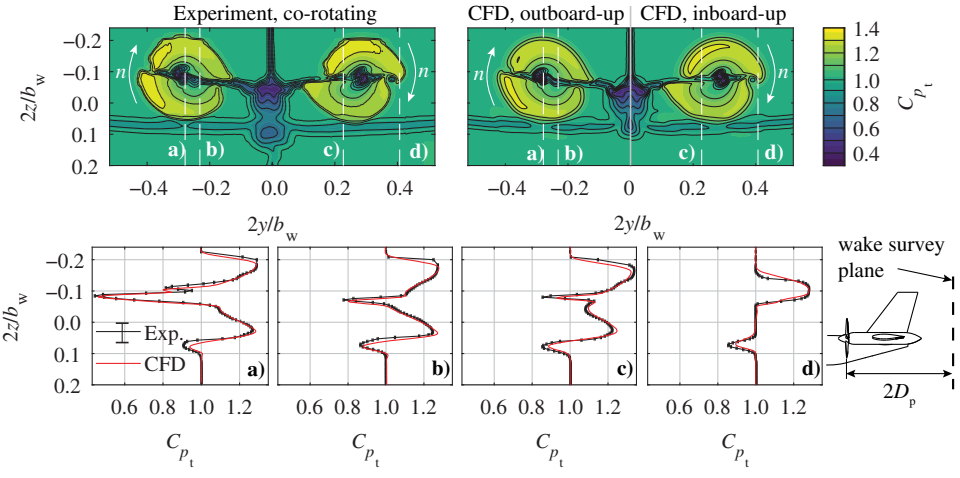

Fig. 6 Measured and computed time-averaged total-pressure distribution in a wake survey plane. Clean configuration, $J = 1.8$, $\alpha = 0$ deg.

IV. Characterization of Aerodynamic Interaction

In this section the time-averaged propeller–airframe aerodynamic interaction is characterized by analyzing the flowfields in the vicinity of the propeller and tailplane that determine the changes in loads. The aerodynamic loads on the propeller are analyzed in Sec. IV.A, followed by the analysis of the aerodynamic forces on the tailplane in Sec. IV.B. The observed trends at a component level are put in perspective on aircraft level in Secs. V and VI. Although the quantitative results are configuration and geometry specific, trends and flow phenomena discussed are considered representative of a typical tail-mounted propeller aircraft application because of the representative conditions and aircraft geometry.

A. Time-Averaged Propeller Loads Induced by the Airframe

The airframe-induced flowfield at the propeller disk is determined by the wing circulation and wake, the upstream effect of the tailplane, and the flowfield induced by the fuselage. As a result of this nonuniform inflow, the installation leads to a shift and to a change in slope of the characteristic propeller curves relative to the ones of the propeller in isolated conditions. For the assessment of the airframe-induced propeller forces, a distinction is made between the types of flowfield at the propeller plane. Stability and performance aspects are relevant for cruise conditions, i.e., the linear region of the lift curve, for which the flowfield can primarily be described as potential flow. For the nonlinear region, where the characteristic flowfield at the propeller is also determined by flow separation, in particular aspects that influence the overall airplane stability are of interest. Both conditions are described separately below.

1. *Cruise Conditions: Linear Part of Lift Curve*

In cruise conditions, the aircraft angle of attack is typically between 0 and 3 deg. In addition to this geometric angle of attack, the propellers operate in the wing-induced downwash field and a fuselage-induced sidewash. The downwash affects the region on the disk with the up- and down-going blades, whereas the sidewash affects the region where the blades have a vertical orientation, schematically shown as quadrants I–IV in Fig. 7a. The difference in loading between each quadrant pair (I&III and II&IV) leads to a side force and a normal force, with the direction determined by the propeller rotation direction, as sketched in Fig. 7b. Because of the unsteady aerodynamics, there is a difference between the phase angle at which the disturbance is encountered and the phase angle at which the change in torque occurs [63,71,81]. Consequently, velocity component w introduces a side force, whereas v introduces a normal force, as depicted in Fig. 7b. The direction of these secondary in-plane forces depends on the propeller rotation direction.

The inflow to the propeller was extracted from the numerical data from the propeller-off simulations. At $\alpha = 0$, the wing downwash angle varies from $\varepsilon = 1$ deg to $\varepsilon = 4$ deg over the propeller disk, schematically shown in Fig. 7a, with the maxima around $z_p/R_p = 0.5$.

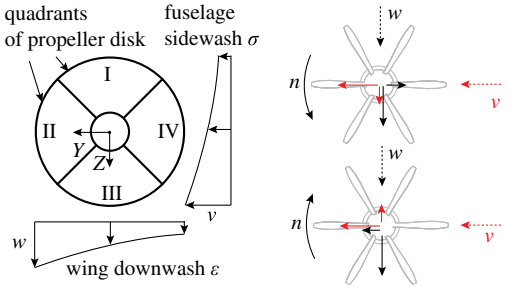

a) Downwash and sidewash distribution

b) Solid red and black arrows indicate in-plane forces due to v and w, respectively.

Fig. 7 Schematic in-plane velocity distributions at $\alpha = 0$ deg that affect the load distribution in the quadrants, leading to a net in-plane force on the port propeller.

The conically shaped aft fuselage induces a sidewash at the propellers, which varies from $|\sigma| = 1$ deg at $z_p/R_p = -1$, to $|\sigma| = 3$ deg at $z_p/R_p = 1$.

To relate the propeller load distribution to the nonuniform inflow, the time-averaged velocity field is expressed as a change in local advance ratio J' consisting of an axial component and tangential component: $J' = J'_a + J'_t$ [71]. Figure 8a depicts the change in local advance ratio extracted from the CFD simulations of the propeller-off condition at $\alpha = 0$ deg. The up-going blades and the blades that move away from the fuselage experience a reduction of the local advance ratio, and therefore higher thrust and torque, as shown in Figs. 8b and 8c, respectively. Such a loading distribution is comparable to the one of a propeller at an angle of attack [71,81], but the distribution is less symmetric for the installed case.

For the installed propeller, the change in out-of-plane velocity was small compared with the total change in advance ratio (Fig. 8a): on average $\Delta J'_a = +0.02$ at $\alpha = 0$ deg. Approximately half of this value is estimated to be from the presence of the wind-tunnel walls (for which the data are not corrected), and the remainder is attributed to the presence of the curved aft-fuselage with the associated pressure field. The dominant inflow perturbation is in the in-plane direction. At a nonzero angle of attack, the inflow to the propeller is a superposition of the geometric inflow and an airframe-induced inflow. The result is that at $\alpha = 5$ deg (Fig. 9a), the magnitude of $\Delta J'$ is significantly reduced compared with the propeller in isolated conditions (Fig. 9b). The regions of higher and lower advance ratios shift approximately 90 deg clockwise for the propeller on the port side. This shift leads to a change in thrust distribution. Relative to $\alpha = 0$ deg, the average change in J_a is negligible, except for the lower side of the disk on which the wing wake impinges. The change in axial inflow is negligible because $\Delta J_a = (\cos\alpha - 1)J_\infty$ is offset by the downwash component $\Delta J_a = J_\infty \sin\alpha \sin\varepsilon$. Furthermore, downstream of the wing at the propeller plane (outside the viscous region), the axial velocity induced by the wing is negligible. Because the perturbations of the in-plane and out-of-plane velocity fields are reduced in magnitude and distributed over the disk for the installed propeller, it follows that the downwash cannot be considered as a pure angle-of-attack effect; i.e., $\alpha_{\text{eff,prop}} \neq \alpha - \varepsilon$.

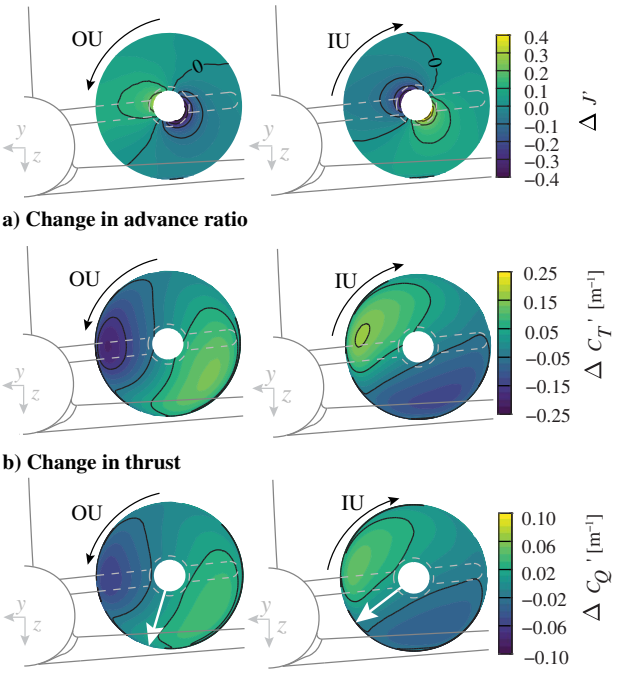

a) Change in advance ratio

b) Change in thrust

c) Change in torque. Arrows indicate the direction of the inplane force

Fig. 8 Effect of airframe installation on the propeller loading at $J_\infty = 1.8$ and $\alpha = 0$ deg, relative to an isolated propeller. CFD results of the clean configuration, $\beta = 0$ deg.

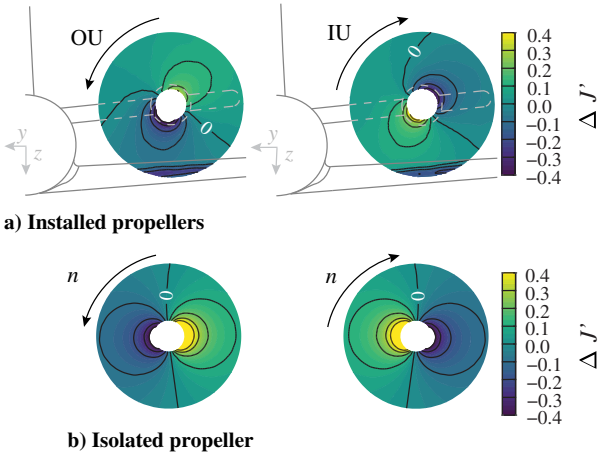

a) Installed propellers

b) Isolated propeller

Fig. 9 Comparison of inflow expressed in local J value at $J_\infty = 1.8$ and $\alpha = 5$ deg for the installed and isolated propeller, relative to $\alpha = 0$ deg. CFD results of the clean configuration, $\beta = 0$ deg.

For the isolated propeller, the thrust increases with angle of attack, as shown in Fig. 10a. Approximately half of this increase is caused by the reduced axial inflow, determined by evaluating the propeller at $J = J_\infty \cos\alpha$. The other half comes from the in-plane velocity component because T_C varies quadratically with J and the thrust rise on the advancing blade is larger than the reduction in thrust on the retreating blade [71].

The installation effect on the integral propeller forces is shown in Fig. 10. The combined in-plane and out-of-plane flowfield causes only a slight reduction in C_T at $\alpha = 0$ deg compared with the same propeller in isolated conditions, depicted in Fig. 10a. As the axial inflow remains nearly constant and the in-plane velocity component that appears at increasing angle of attack is compensated by the downwash, in the installed configuration, C_T is less dependent on α than in the isolated configuration.

The installation also changes the in-plane forces, as shown in Fig. 10b. The $C_{Y_p} - \alpha$ curve is shifted, primarily as a result of the sidewash that leads to a side force toward the fuselage symmetry plane. The shift is larger for the inboard-up rotating propeller because for that case the downwash causes an additional side force in the same direction as the one induced by the fuselage. The gradient C_{Y_α} for the outboard-up propeller is higher than the one for the isolated propeller for two reasons. First, the average wing-induced downwash at the propeller disk increases with angle of attack because the maximum downwash angle shifts in negative z direction in the propeller plane. The side force associated with the wing downwash therefore increases with angle of attack. Second, with increasing angle of attack, the impinging wing-wake around $z_p/R_p = 1$ also leads to a side force that acts in the same direction as the one that is induced by the fuselage sidewash. The opposite is the case for the inboard-up rotating propeller, hence its lower slope compared with the isolated propeller.

The propeller normal-force curves for both rotation directions are shifted up and their slope is reduced compared with the isolated propeller. The gradients of the normal-force curve, $C_{N_{p,\alpha}}$, are lowered by −27 and −17% compared with the isolated propeller for the outboard-up and inboard-up propeller, respectively. This reduction is a consequence of the propeller experiencing a downwash gradient $d\varepsilon/d\alpha$ from the wing and fuselage that increases with angle of attack from on average 0.15 at $\alpha = 0$ deg to 0.25 at $\alpha = 5$ deg. These values indicate that by taking the average downwash gradient, the propeller normal force can be predicted with reasonable accuracy, even though the maximum value of this gradient shifts upward (in negative Z direction) with angle of attack. The difference between the two rotation directions is primarily caused by the increasing sidewash with angle of attack, which makes C_{Z_p} more positive for the outboard-up rotating propeller, hence reducing $C_{Z_{p,\alpha}}$ for this rotation direction. The offset at $\alpha = 0$ deg is larger for the outboard-up rotating propeller as the airframe-induced sidewash positively contributes to C_{Z_p} for this rotation direction.

The axial velocity field is responsible for a negligible difference in propeller efficiency at $\alpha = 0$ deg, as shown in Fig. 10c. For the isolated propeller, the propeller efficiency slightly increases with increasing the angle of attack due to the lower axial inflow and the in-plane velocity component. In line with the moderate increase in thrust due to the lower effective advance ratio when installed, the efficiency is nearly independent of angle of attack for the cruise condition. For $\alpha > 5$ deg, the efficiency increases due to the installation as the result of the wake impingement.

In summary, the installation effects of the propeller forces in cruise condition are not negligible. The largest difference with the uninstalled propeller is a reduced gradient of the propeller normal force with angle of attack. The observed differences between the two rotation directions are caused by the translation of the maximum downwash gradient with angle of attack and by the different response to the fuselage-induced sidewash.

2. *High-Lift Conditions: Effect of a Flap Deflection*

In addition to the fuselage and main wing induced flowfield, a flap deflection leads to an additional nonuniform inflow to the propellers. The measured total-pressure field behind the aircraft at $\alpha = 0$ deg with a 27 deg flap deflection is depicted in Fig. 11a. The figure shows a strong flap-edge vortex that induces a swirling inflow on the inboard and lower part of the propeller disk, in addition to a strong downwash of approximately 16 deg. It is apparent from the region of increased total pressure that the thrust distribution is highly affected in this condition in comparison to the case without a flap deflection, as shown in Fig. 6b. The resulting effect on the integral propeller forces is depicted in Fig. 11b. With the flap installed, also $d\varepsilon/d\alpha$ increases due to higher induced losses and a higher lift curve slope. Consequently, the slope of the propeller normal-force curve with angle of attack reduces approximately 50% compared with the clean condition. Moreover, the larger downwash angle at $\alpha = 0$ deg leads to a significant force on the propellers in negative Z direction, which affects the trim condition. The thrust is found to remain nearly independent of flap deflection.

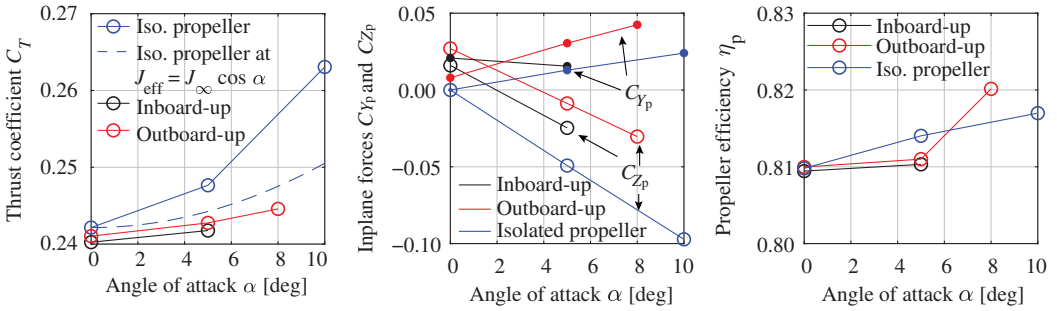

a) Propeller thrust

b) In-plane forces C_{Y_p} and C_{Z_p}

c) Propeller efficiency

Fig. 10 Computed changes in forces due to installation on the port propeller, $J = 1.8$. CFD results of the clean configuration, $\beta = 0$ deg.

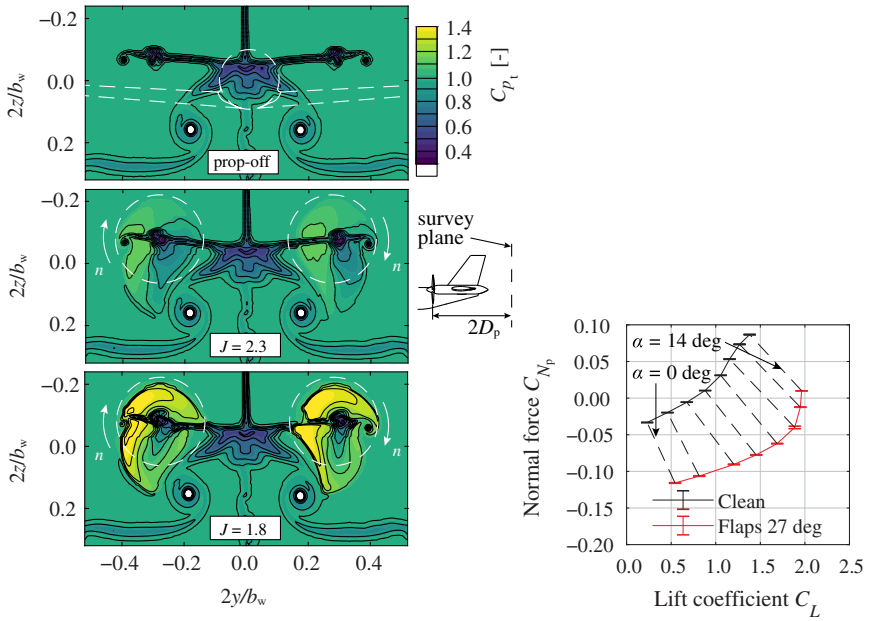

a) Measured total pressure downstream at $\alpha = 0$ deg **b) Normal-force coefficient of port propeller, outboard-up rotation, $J = 2.3$**

Fig. 11 Effect of a flap deflection of $\delta_f = 27$ deg on the propeller slipstream development and propeller normal force. Experimental results, $\beta = 0$ deg.

3. High-Lift Conditions: Angle-of-Attack Effect

The installation effect on the propeller forces up to $\alpha = 8$ deg in the clean configuration is moderate and is nearly linear with angle of attack, as shown in Fig. 10. By increasing the angle of attack further into the nonlinear region of the aircraft lift curve, the propeller thrust rises rapidly over the complete range of advance ratios, in particular for the outboard-up rotating propeller, as shown in Fig. 12. This behavior can be understood by assessing the flowfield at an angle of attack of $\alpha = 14$ deg, as shown in Fig. 13a. In this condition, the maximum changes in local advance ratio at the propeller disk are $\Delta J' = -1.8$ and $\Delta J' = +0.6$ for the outboard-up and inboard-up configurations, respectively. Based on the performance curves of the isolated propeller [71], these values indicate that the blades experience either wind milling conditions or separated flow, and the blades for both rotation directions experience significant time-dependent inflow. An appreciable part of the reduction in advance ratio, up to $\Delta J'_a = -0.6$, comes from the deficit in total pressure by the separated flow from the wing root that impinges on part of the propeller disk.

The significant difference in thrust between the rotation directions is caused by the in-plane velocity components. The regions of positive and negative axial vorticity in and adjacent to the propeller plane, shown in Fig. 13b, are indicative of circulation that changes the inflow encountered by the blades. The cause of the negative

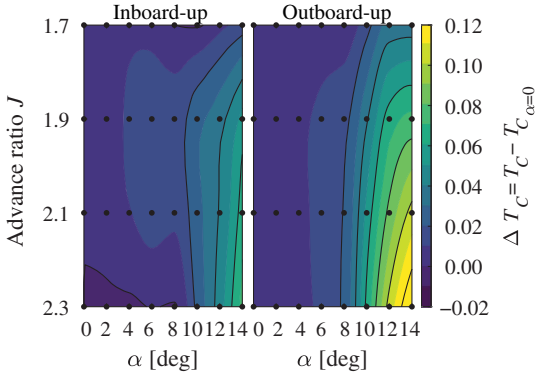

Fig. 12 Installation effect on propeller thrust at increasing angle of attack. The black dots indicate the measurement points. Experimental results of the clean configuration, $\beta = 0$ deg.

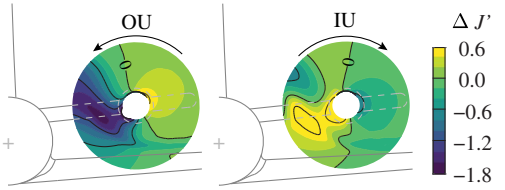

a) Change in local advance ratio relative to isolated conditions at $\alpha = 0$ deg, $J_\infty = 1.8$

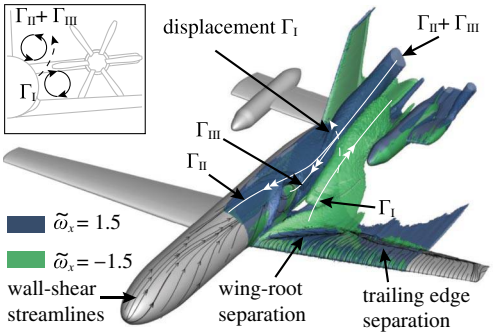

b) Illustration of the vortex formation. Flowfield only shown for $y < 0$

Fig. 13 Nonuniform inflow to the propeller at $\alpha = 14$ deg, propellers-off. CFD results of the clean configuration, $\beta = 0$ deg.

component of the axial vorticity $\tilde{\omega}_x$ is the significant drop in wing lift from the wing–fuselage junction up to 40% span, which sheds a sheet of trailing vorticity that rolls up into a strong vortex opposite in sign to the wing-tip vortex, indicated by Γ_I in Fig. 13b. From the isosurfaces of vorticity depicted in the same figure, two more vortices can be distinguished that are opposite in sign to Γ_I. First, a vortex is formed on each side of the fuselage [82], originating close to the fuselage nose, denoted by Γ_{II}. Secondly, the root separation leads to a pressure gradient along the fuselage [83] that results in a vortex denoted by Γ_{III}. This pair of corotating vortices rapidly merge into a single vortex ($\Gamma_{II} + \Gamma_{III}$) that is counter-rotating to Γ_I and contains approximately three times the circulation of Γ_I. The relative distance and strength are such that vortex Γ_I displaces in vertical direction and toward the symmetry plane of the aircraft, over a relatively short distance [84]. The net effect of the vortex pair is a significant in-plane

velocity component, equivalent to the large change in J', depending on rotation direction. In particular the outboard-up rotating propeller experiences a large reduction in advance ratio, as the propeller rotation is opposite to the resulting swirling inflow, and is further reduced by the deficit in total pressure.

Next to the rise in thrust, the vortex-induced inflow also leads to a large normal force that is in negative Z direction for the outboard-up rotating propeller, whereas it is in opposite direction for the inboard-up rotation direction. The location where the swirling inflow impinges the propeller depends on angle of attack and angle of sideslip. Additionally, the magnitude of this swirl is dependent on the aircraft attitude. The propeller contribution to overall aircraft stability and trim therefore varies with angle of attack if such a swirling inflow impinges on the propeller or is in the vicinity of the propeller disk. It is found that $C_{N_{p,\alpha}}$ increases up to three times the value that corresponds to the one at $\alpha = 0$ deg for the outboard-up rotating propeller, and reduces up to $C_{N_{p,\alpha}} = 0$ for the inboard-up rotating propeller, as indicated in the figures provided as Supplemental Materials S5.

An improved fairing design compared with one of the models analyzed in the current paper would reduce the flow separation at the wing–fuselage junction and therefore the relative strengths of the separation-induced vortices. However, the qualitative development of the flow reversal is still representative, since it has been identified in previous studies [82,85] and occurs to some extent at any wing–root junction.

In summary, the separated flow from the wing–fuselage junction, present at high angle of attack for the configuration considered herein, significantly influences the propeller forces. The swirling character of this flowfield in particular leads to an increase in thrust and propeller normal force for the outboard-up rotating propeller and thus a stabilizing contribution at aircraft level, whereas the inboard-up rotating propeller has approximately no stabilizing contribution at aircraft level in these conditions.

B. Time-Averaged Tailplane Loads Induced by the Propeller

The aerodynamic forces on the horizontal tailplane affect the aircraft trim and stability characteristics. In terms of performance, in particular the change in drag characteristics and the offset in the normal-force curve are of interest, as these influence the aircraft drag in trimmed conditions. From a stability and control perspective, primarily the gradient of the normal-force curve $C_{N_{ht,\alpha}}$, in this paper referred to as the effectiveness of the tail, and elevator effectiveness $C_{N_{\delta_e}}$ are relevant quantities, of which the integral forces and load distributions are depicted in Fig. 14.

The effect of propeller installation on tailplane forces is quantified relative to the propeller-off condition. Figure 14a shows the normal force distribution in the propeller-off condition. It is noted that normal force should not be mistaken as the lift force (despite lift being the dominant factor): at a nonzero angle of attack, the tailplane drag also enhances the force normal to the tailplane. At $\alpha = 0$ deg, there is a downforce on the tailplane due to the wing downwash. The presence of the fuselage leads to a drop in $c_{n_{ht}}$ near the tail–fuselage junction, such that a vortex is shed that is opposite in sign to the tip vortex. The added normal force distributions by the inboard-up and outboard-up propeller installations, shown in Fig. 14b, are typical for an aerodynamic surface behind a propeller: the direction of the local swirl determines the direction of the change in lift force, and the spanwise variation of circulation redistributes the additional load in spanwise direction such that the changes are not confined to the region where the slipstream impinges on the tailplane [86]. For both rotation directions, the largest change in normal force occurs on the inboard part of the tailplane. This can directly be related to the distribution of gradient of tailplane normal force with respect to angle of attack, $c_{n_{ht,\alpha}}$, of the propeller-off condition. This normal force gradient reduces toward the tip because of the tip-relief effect. For the propeller-off case, the average of $c_{n_{ht,\alpha}}$ over the outboard part of the span ($2y/b_{ht} > 0.7$) is 39% lower than the one for inboard part of the span ($2y/b_{ht} < 0.7$). The combination of this varying $c_{n_{ht,\alpha}}$ and

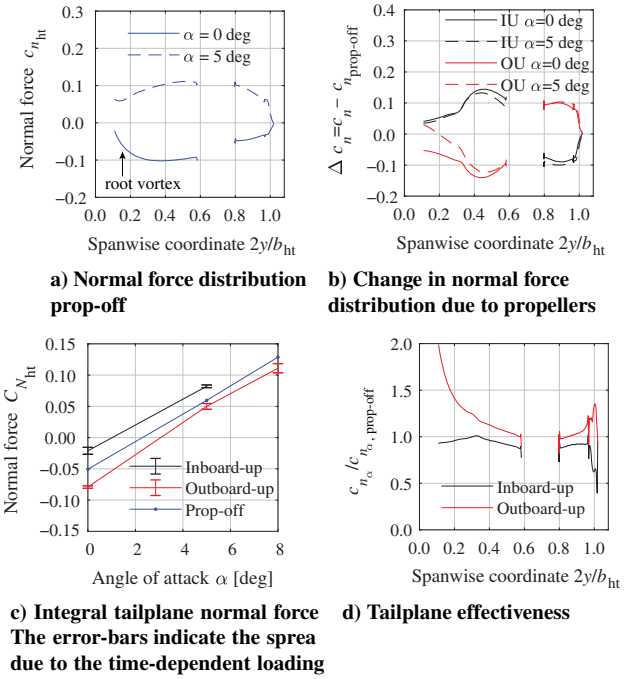

a) Normal force distribution prop-off

b) Change in normal force distribution due to propellers

c) Integral tailplane normal force The error-bars indicate the sprea due to the time-dependent loading

d) Tailplane effectiveness

Fig. 14 Effect of propeller installation on the tailplane load distributions and integral forces, $J = 1.8$. Coefficients normalized with tailplane area and chord. CFD results of the clean configuration, $\beta = 0$ deg.

the higher dynamic pressure in the slipstream leads to a net normal force on the tailplane with the direction depending on rotation direction, shown in Fig. 14c. Besides the offset at $\alpha = 0$ deg, the gradient $C_{N_{ht,\alpha}}$ relative to the propeller-off condition is 17% higher for the outboard-up configuration, whereas the inboard-up rotation shows a 7% reduction. The difference between the two rotation directions is a combination of the downwash distribution, which is a function of the vorticity shed by the tailplane and the varying inflow with angle of attack. Figure 14d reveals that the tailplane sections toward the root are especially affected by the propeller installation, as locally $c_{n_{ht,\alpha}}$ is twice the value of the propeller-off condition, even though this is outside of the region on which the propeller slipstream impinges.

The hyperbolic character of $c_{n_{ht,\alpha}}$ for the outboard-up rotation indicates that the vortex stemming from the tailplane–fuselage junction is manipulated by the propeller. A schematic of the tailplane vortex system is shown in Fig. 15a. The vortex shed from the tailplane–fuselage junction is indicated as Γ_I and its direction is opposite to the tip vortex, denoted by Γ_{III}. The gradient of the circulation along the span also sheds a vortex Γ_{II} at the nacelle. These vortices can also be distinguished in the axial vorticity distribution downstream of the model, shown in Fig. 15b. With the installation of the propeller, two vortex systems can be identified: a helical vortex system from the propeller and the shed vorticity from the tailplane. Conceptually, the combined propeller–tailplane vortex system can be simplified as schematically shown in Fig. 15a: a tailplane root-vortex (Γ_A), a vortex around the tip vortex impingement (Γ_B), a vortex shed at the propeller rotation axis (Γ_C), the tailplane tip vortex (Γ_D), the propeller hub-vortex, and the circular sheet containing the vorticity shed by the propeller tips. In addition to the local swirl induced by the propellers, the relative strength and direction of this vorticity dictate the local downwash distribution and the rate at which these change with angle of attack partially determines $c_{n_{ht,\alpha}}(y)$.

For the outboard-up rotation, $d\Gamma_A/d\alpha$ is opposite to $d\Gamma_I/d\alpha$ and $d\Gamma_C/d\alpha$ is opposite to $d\Gamma_{II}/d\alpha$. The net result is that on the inboard part of the tailplane, the outboard-up rotation leads to a smaller downwash. The opposite is the case for the inboard-up rotation direction. The consequence is that, for the outboard-up case, the root vortex shed from the tail is nearly inexistent if the angle of attack is increased from 0 to 5 deg. At the tip of the tailplane, the axial

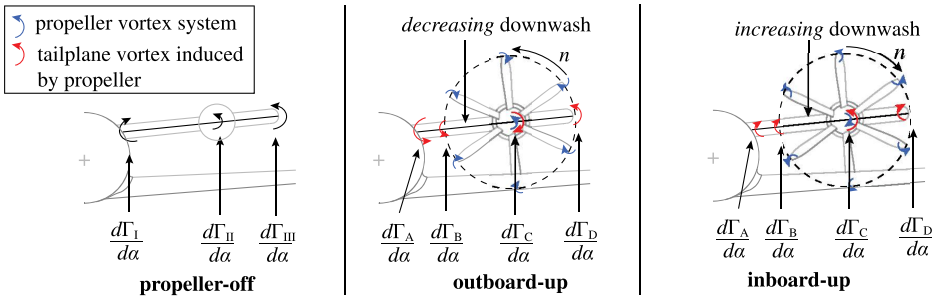

a) Schematic of the propeller and tailplane vortices and their rate of change with angle of attack

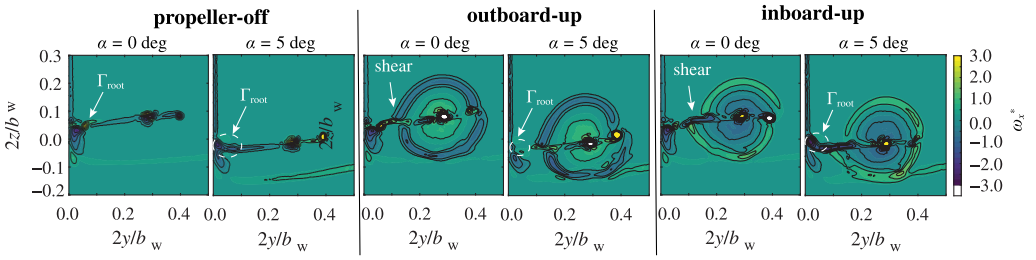

b) Time-averaged normalized axial vorticity in a plane at $X = -2D_p$ (CFD results)

Fig. 15 Propeller–tailplane vortex structures at low angle of attack to identify the relative strength and the direction of the trailing vorticity from the tailplane due to propeller installation. CFD results of the clean configuration, $\beta = 0$ deg.

component of the propeller tip vortex is opposite in sign to the tip vortex of the tailplane for the inboard-up rotating propeller (contrary to a propeller that is mounted on the tip of the horizontal tailplane). The net effect is locally a higher induced loss, hence a lower $c_{n_{ht,\alpha}}$ in the tip region, confirmed by the distribution depicted in Fig. 14d. It is therefore concluded that the particular position of the propeller relative to the root and tip vortex of the tailplane is such that the typical trend of a higher C_{L_α} for an inboard-up rotating propeller (see Ref. [41]) does not hold.

To determine to what extent the changing slipstream quantities with angle of attack influence the observed changes of $C_{N_{ht,\alpha}}$ in Fig. 14d, the time-averaged flowfield is analyzed in a plane between the propeller and tailplane, depicted in Fig. 16. The regions with a higher propeller loading locally lead to a higher total pressure, a higher dynamic pressure, and a larger swirl angle in the slipstream. The figure shows the slipstream quantities along a survey line on the inboard part of the tailplane. By increasing $\alpha = 0$ deg to $\alpha = 5$ deg, ΔC_{p_t} changes with ± 0.1 and a maximum change in swirl angle of ± 1 deg is observed due to the higher thrust and torque, respectively. The local swirl angle alters the local inflow angle α'. Therefore, an outboard-up rotation results in $(dC_{p_t}/d\alpha) > 0$ and $(d\alpha'/d\alpha) < 0$, whereas for the inboard-up rotation it is the inverse. Compared with an increase of dynamic pressure by $\Delta q_s = \pm 0.1 q_\infty$, the angle of attack change of ± 1 deg is the primary factor to change the lift of a two-dimensional airfoil section. It follows that the rate at which the slipstream changes on the inboard part of the tailplane yields a trend opposite to the one observed in Fig. 14d: for the outboard-up rotating propellers the swirl and dynamic pressure increase, which reduces C_{N_α}. Therefore, the observed trends of C_{N_α} are attributed to the interaction of the propeller vortex system with the tailplane and not to the changing slipstream characteristics with angle of attack.

The drag force on the tailplane is influenced by the propellers, depicted in Fig. 17. The friction drag increases due to the higher dynamic pressure in the slipstream. The induced drag changes as the added force vector is titled relative to the freestream because of the swirl in the slipstream and due to the altered variation of circulation along the tailplane span. A swirl that locally enhances the normal force that exists in the propeller-off condition locally leads to a larger swirl-recovery by the tailplane [86]. Therefore at $\alpha = 0$ deg, there is a reduction of tailplane drag on the side of the downgoing blades as the tailplane in propeller-off condition produces a force in positive z direction, as shown in Fig. 14a. At $\alpha > 0$ deg, the drag reduction

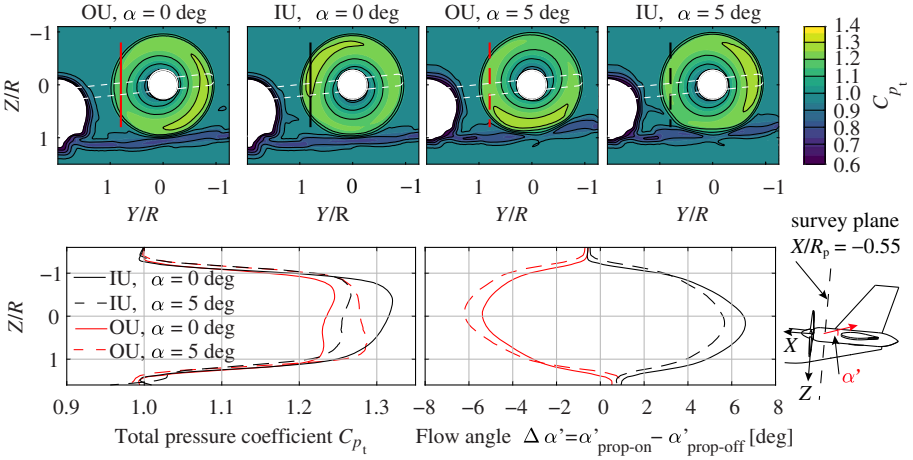

Fig. 16 Time-averaged flowfield between the propeller and horizontal tail for two angles of attack at $T_C = 0.18$ and $J = 1.8$. CFD results of the clean configuration, $\beta = 0$ deg.

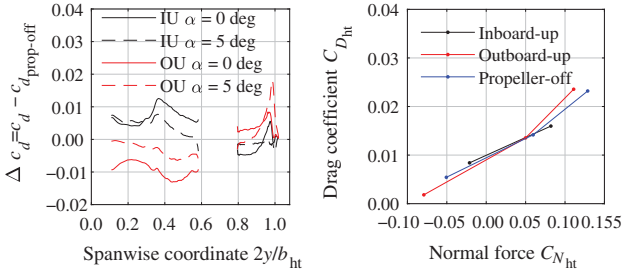

a) Drag distribution b) Tailplane efficiency

Fig. 17 Effect of propeller installation on the tailplane drag, $J = 1.8$. Coefficients normalized with tailplane area and chord. CFD results of the clean configuration, $\beta = 0$ deg.

becomes less for the outboard-up rotating propeller. For this reason, depending on the combination of the sign of $C_{N_{ht}}$ and propeller rotation direction, the drag is higher or lower relative to propeller-off condition, as depicted in Fig. 17b. For a trimmed flight, where typically $C_{N_{ht}} < 0$, an outboard-up rotating configuration leads to the lowest tailplane drag. Consequently, for a corotating configuration, the difference in tailplane drag leads to a yawing moment.

In summary, the particular location of the propeller on the tailplane leads to the manipulation of the vortex from the tailplane–fuselage junction that causes the tailplane to be more effective if the propeller is rotating outboard-up at angles of attack that are representative for the cruise condition. An inboard-up rotating propeller leads to a lower effectiveness of the tailplane relative to the propeller-off case.

V. Installation Effect on Static Stability and Control Characteristics

In the previous section the propeller–airframe aerodynamic interaction was discussed at a component level. Those findings are put into perspective in this section by assessing the impact on the aircraft pitching and yawing-moment coefficients.

A. Longitudinal Stability

The derivative of the propeller normal force with angle of attack (Fig. 10b) enhances the aircraft longitudinal stability because the propellers are behind the aircraft center of gravity, whereas the contribution of the change in tailplane loading due to the propeller depends on the rotation direction and aircraft angle of attack. The resultant effect on pitching-moment curve is depicted in Fig. 18a for the clean configuration with corotating propellers. For the full range of angles of attack, the propeller installation has a relatively small effect on pitching moment compared with the propeller-off condition. At the thrust setting that is representative for approach conditions ($J = 2.3$, $T_C = 0.03$), the neutral point shifts rearward relative to the propeller-off condition with $(\Delta x/\bar{c}) = -0.05$ at low angles of attack, up to $(\Delta x/\bar{c}) = 0.00$ at $\alpha = 7$ deg. At higher thrust settings, the rearward shift is larger. As the most forward location of the neutral point is at low angle of attack in the clean configuration, which is therefore the most critical of all flight conditions in terms of stability, the overall stability is not adversely affected, which is in line with the findings of Ref. [87]. In Supplemental Materials S6 the curves at constant advance ratio are plotted for the clean configuration and for two high-lift conditions.

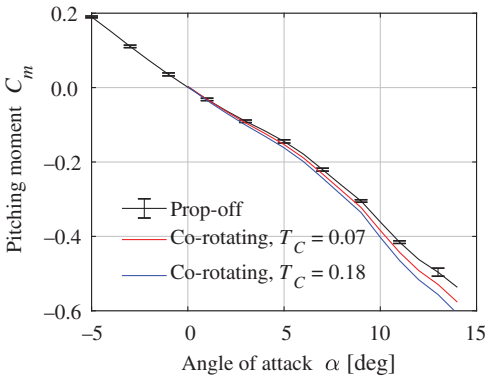

a) Pitching moment vs. angle of attack for the clean configuration. Data points at constant T_C are obtained by data fitting.

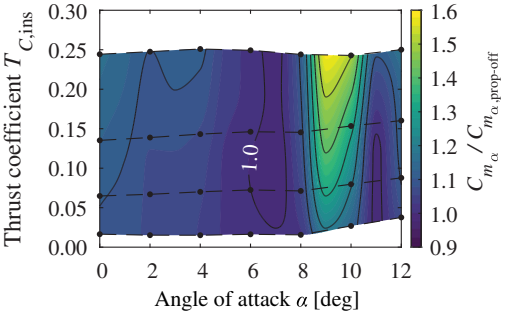

b) Change in C_{m_α} by inboard-up propeller installation, clean configuration. Dashed lines represent constant advance ratio.

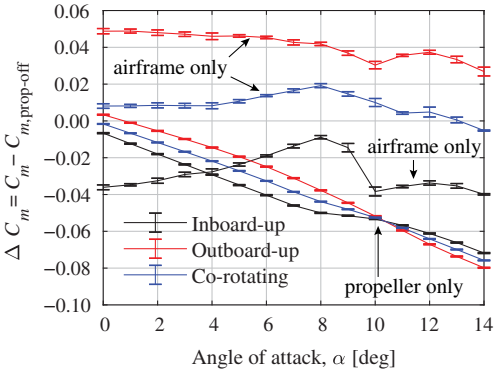

c) Change in pitching moment at $J = 1.8$, clean configuration. Airframe and propeller contributions split-up.

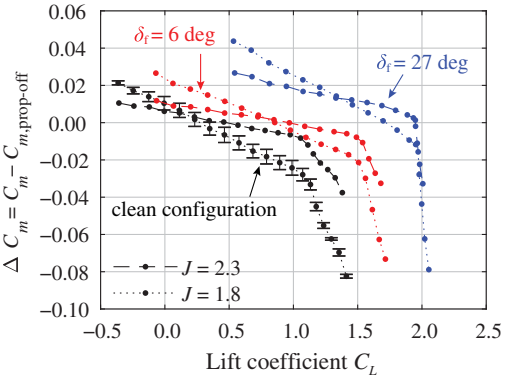

d) Change in pitching moment with lift coefficient co-rotating propellers.

Fig. 18 Effect of the propeller installation on the aircraft pitching moment about $0.25\bar{c}$. Experimental results, $\beta = 0$ deg. Limited number of error bars are plotted to improve readability.

The relative longitudinal stability, $C_{m_\alpha}/C_{m_\alpha,\text{prop-off}}$, is shown in Fig. 18b for the inboard-up configuration. It varies between 1.0 and 1.4, whereas smaller variations of 1.0–1.25 are induced by the outboard-up configuration. The contour plot shows that for a given α, increasing T_C only leads to a moderate change in pitch stability, contrary to a change in α, which has a significant impact on longitudinal stability. The large variations of C_{m_α} start from the onset of the nonlinearity of the lift curve, i.e., $\alpha > 5$ deg.

To determine the relative contribution of the airframe and propeller to the pitching moment, the measured propeller forces are subtracted from the external balance measurements and the contributions to pitching moment are plotted in Fig. 18c. As expected from the C_{N_p} curves discussed in Sec. IV.A, the propeller has a stabilizing contribution, in particular if it is rotating outboard-up. In line with the propeller in isolated conditions, the normal force contribution to the aircraft moment is nearly independent of thrust. The C_{m_p} curves are approximately linear up to $\alpha = 8$ deg, followed by a decrease and increase for the inboard-up and outboard-up rotating propellers, respectively, as a result of their nonuniform inflow, as discussed in Sec. IV.A. Of the propeller-induced pitching moment, the largest contribution is the propeller normal force (shown in the breakdown of each propeller force and moment component in Supplemental Materials S7). Despite a varying thrust with angle of attack, the thrust yields approximately a constant offset of $C_m - \alpha$, as its moment arm is relatively small. The pitching moment about the propeller Y axis has a negligible contribution.

In Sec. IV.B it was shown that the inboard-up and outboard-up rotation decrease and increase the normal force gradient of the tailplane, respectively. This is reflected in Fig. 18c as a destabilizing airframe contribution to the moment coefficient up to $\alpha = 8$ deg for the inboard-up rotation, whereas the contrary is the case for the outboard-up rotating configuration. The corotating propeller installation is nearly the average of the two rotation directions, which indicates that the aerodynamic coupling between the two sides of the horizontal tailplane is negligible. The rapid change of the airframe contribution to C_{m_α} at $\alpha = 8$ deg, in particular with the inboard-up configuration, is a consequence of two aspects. Firstly, the rapid reduction in C_{m_p} for the inboard-up propeller indicates that the loading on the upgoing blade is increased because of the loss in wing lift at these spanwise locations, and therefore a lower gradient of the wing downwash is generated. The consequence is locally a higher swirl and dynamic pressure at the inboard part of the tailplane, leading to a stabilizing normal force, and hence a more negative C_{m_α}. The second aspect is that the fuselage-induced vortex in streamwise direction (Γ_{II} in Fig. 13b), which initiates between $\alpha = 5$ deg and $\alpha = 8$ deg, is altered by the propeller installation. Around $\alpha = 8$ deg, these two vortices are situated slightly above the tailplane, near the junction with the fuselage. The inboard-up rotating propeller leads to an opposite vortex at the tailplane–fuselage junction, which is thereby reducing the influence of Γ_{II} on the tailplane.

Besides the changes in the slope of the moment curve, also the propeller-induced shift of the curve is relevant as it influences the trim condition. As discussed in Sec. IV.A.2, a flap deflection results in a nose-up moment due to the larger propeller normal force in Z direction at the same lift coefficient, as shown in Fig. 18d for the corotating configuration. These shifts in C_m indicate that a trim scheduling is required to maintain a constant lift coefficient that should be a function of thrust coefficient and flap setting. On the other hand, the significant nose-down pitching moment from the flaps (Fig. 18a) is partially offset by the propeller installation. It follows that a smaller elevator deflection is required to trim the aircraft. The figure also shows that the overall installation effect of two corotating propellers on the pitching moment is an offset and a nearly constant change in slope up to the nonlinear region of the lift curve, where the slope changes rapidly and remains approximately constant again for the higher angles of attack.

B. Longitudinal Control and Trim

In the previous section, it was shown that the circulation on the tailplane in propeller-off condition partially determines how the loading is affected if the propeller is installed. Alternatively to altering the angle of attack, an elevator deflection also affects the tailplane circulation distribution. The effect of the propeller installation for a positive elevator deflection is depicted in Fig. 19, using $0.25\bar{c}$ as the moment reference point. For a given angle of attack, the elevator effectiveness $C_{m_{\delta_e}}$ increases with T_C due to the rise of dynamic pressure in the slipstream, as shown in Fig. 19a. At constant J (and approximately constant T_C), $C_{m_{\delta_e}}$ is nearly independent of angle of attack for the corotating configuration. The trends observed in Fig. 14c for the inboard-up and outboard-up configurations are in line with the lower and higher normal force gradients of the tailplane, respectively.

The necessary trim input to compensate for the offset and change in slope of the aircraft C_m curve due to the propeller installation is partially offset by the higher elevator effectiveness. In Fig. 19c it is shown that for a relatively high thrust setting, the required trim input as a result of propeller installation remains within ± 2 deg compared with the propeller-off condition. A lower thrust setting leads to smaller required trim inputs. Therefore, a thrust input at a constant C_L and V_∞ needs to be coupled with an elevator input to maintain the same pitching moment.

C. Directional Stability and Trim

The directional stability and trim are influenced by the propeller installation in three ways. First, the propellers introduce a yawing moment due to their distance from the moment reference point. Second, the airframe induces a nonuniform inflow to the propeller, which affects the propeller forces and thus their contribution to the moments. Finally, the (sheared) propeller slipstream introduces sidewash on the aft-fuselage and vertical tailplane [45,50,88]. An overview of these installation effects on aircraft level is depicted in Fig. 20. Figure 20a shows the gradient of the yawing moment with sideslip angle, relative to the propeller-off configuration. The same figure also depicts the yawing moment caused if a propeller in isolated conditions is positioned at the same (x, y, y) location as the installed propellers, using data of Ref. [71]. Nearly independent of thrust coefficient, the propeller installation enhances the

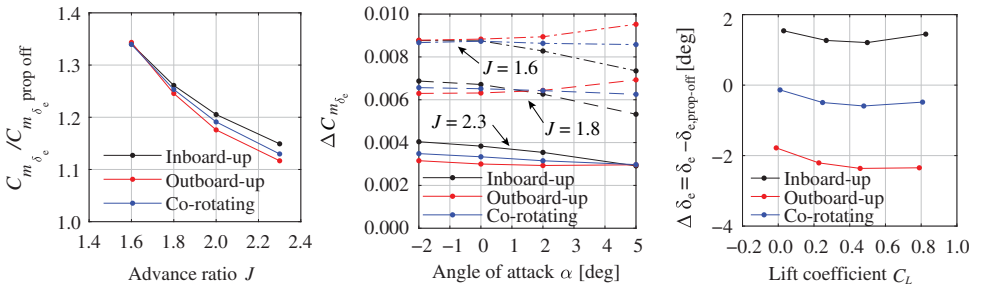

a) Effect of propeller setting on elevator effectiveness $\alpha = 0$ deg

b) Increase of elevator effectiveness

c) Elevator deflection required at $T_C = 0.28$ to maintain $C_{m_{\text{prop-off}}}$

Fig. 19 Effect of propeller installation on elevator effectiveness. Gradients determined over $\delta_e = 0$ deg and $\delta_e = +15$ deg. Experimental results of the clean configuration, $\beta = 0$ deg.

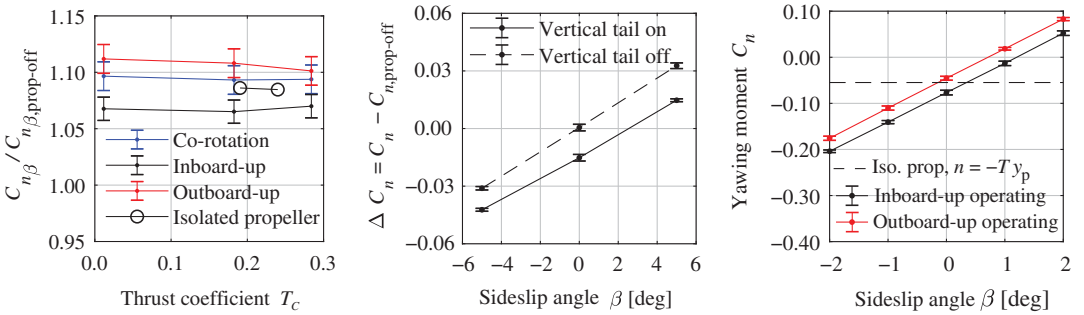

a) Installation effect on C_{n_β}, evaluated over $\beta = \pm 5$ deg

b) Effect of co-rotating propellers on the vertical tail, $T_C = 0.28$.

c) Effect of one-engine-inoperative condition on yawing moment, $T_C = 0.28$. Inoperative port propellers replaced by a dummy spinner.

Fig. 20 Effect of propeller installation on directional stability and yawing moment. Experimental results of the clean configuration, $\alpha = 0$ deg.

directional stability by approximately 6–12%, where the corotating configuration can be approximated by the side force of two isolated propellers. This nearly constant increase is the result of the small variation of the propeller side force with thrust at a given angle of attack. Therefore, also the derivative is nearly independent of propeller thrust.

The corotating configuration shows a similar increase in aircraft C_{n_β}, as the ΔC_{n_β} is caused by two isolated propellers with a moment arm of x_p. This indicates that the direct propulsive effect, i.e., a propeller at an axial distance to the reference point, is the primary contributor to C_{n_β}. Although this direct effect is dominant, there is a distinct difference between the two propeller rotation directions. The difference between the curves is the installation effect, partially coming from the changes in forces on the airframe, and partially due to the different forces acting on the propeller. The latter is attributed to a fuselage-induced nonuniform inflow to the propeller, schematically shown in Fig. 21. The fuselage induces an in-plane flowfield such that the regions (a) and (b) translate in opposite direction to the side force on the vertical tail ($F_{y_{vt}}$), whereas (c) and (d), as a pair, translate in the same direction as $F_{y_{vt}}$. The consequence is an enhanced and reduced C_{n_β} for an outboard-up and inboard-up configuration, respectively.

Besides the forces on the propeller, the presence of a slipstream on each side of the vertical tail also influences the contribution of the vertical tail to the yawing moment. There is a sidewash at the vertical tail for the corotating configuration, also observed in, e.g., Ref. [89]. This flowfield results in an offset of the $C_n - \beta$ curve as a function of thrust, equivalent to a sideslip angle of approximately 2 deg for $T_C = 0.28$, as shown in Fig. 20b. Without the vertical tail, the yawing-moment coefficient is zero at $\beta = 0$ deg, indicating that the propeller-induced sidewash primarily affects the vertical tail. Moreover, the difference in drag on each side of the horizontal tailplane and the lateral shift of the thrust vector due to the propellers operating in the wing downwash field are therefore compensating,

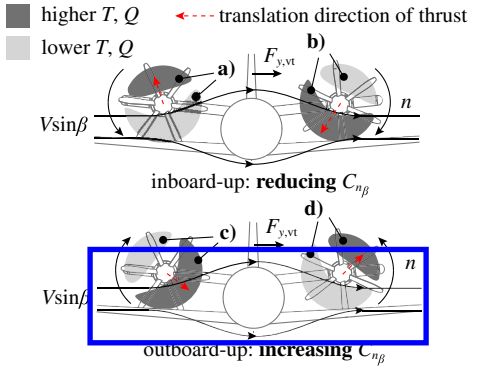

Fig. 21 Lateral shift of thrust vector induced by the fuselage. Letters indicate the pairs of higher and lower propeller thrust and torque.

leading to a net zero effect on yawing moment. Figure 20b also indicates that the installation of the vertical tail partially offsets the increased directional stability stemming from the propellers. This reduction is attributed to the position of the vertical tail between two slipstreams. The dynamic pressure and the effective inflow at the vertical tail are both reduced with an increasing thrust setting, which leads to a reduction of $C_{n_{\beta_{vt}}}$ of 2.5% compared with zero thrust.

For the one-engine-inoperative condition, the yawing moment introduced by the operating propeller needs to be compensated by a rudder deflection. Figure 20c depicts the yawing moment as the result of the port propeller not operating, as well as the moment that is introduced as thrust multiplied with the moment arm, $n = -Ty_p$. As expected, the sidewash on the vertical tail introduced by the outboard-up rotating propeller is opposing the thrust-induced yawing moment. If the outboard-up propeller is inoperative, the sidewash adds to the yawing moment and a larger rudder input is required to trim the aircraft at zero sideslip angle. Hence, the outboard-up propeller is the critical engine.

VI. Installation Effect on Aircraft Performance Indicators

The previous sections have indicated that the propeller installation effects do not adversely affect the aircraft longitudinal and directional stability, and control effectiveness. If the interaction effects are included in the analysis and design at aircraft level, the known drawback of the configuration in terms of added mass [6,56,90] may be slightly offset by the opportunity of resized stabilizing surfaces. However, even for a suboptimal design, indicators such as propeller efficiency in the direction of flight, the airframe lift-to-drag ratio, trim drag, and maximum lift coefficient are already indicative of performance changes due to the propeller installation.

The product $\eta_p(C_L/C_D)$ can be used as a measure of the fuel consumption [91], as it appears in the classical Brequet-range equation, if η_p is assumed not to change with the aircraft attitude. To show the importance of including the interaction in performance prediction, the propeller and airframe efficiencies are assessed separately. The propeller efficiency map, i.e., $\eta_p - \alpha$, is depicted in Fig. 22a for the two rotation directions. As expected, the efficiency along the propeller rotation axis slightly increases with angle of attack, with a maximum for the inboard-up rotating case around $J = 1.9$, close to the advance ratio at which the isolated propeller has its maximal efficiency. Approximately the same trend is followed by the outboard-up rotating propeller. However, the reduction of η_p at $\alpha = 8$ deg, corresponding to the condition with swirling inflow, is only present for the inboard-up rotating propeller, because it operates locally at a higher effective advance ratio. The efficiency of the outboard-up rotating propeller continues to increase up to values close to unity. These high efficiencies are possible because η_p is defined with V_∞, while there is kinetic energy deposition induced by the airframe at the propeller plane.

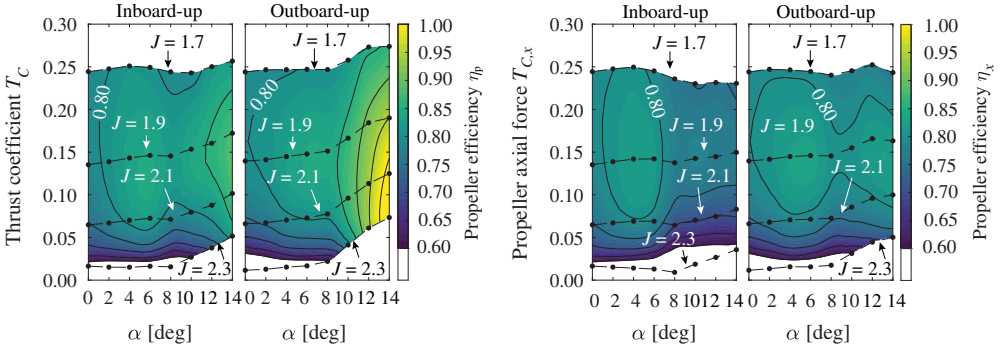

a) Propeller efficiency, η_p b) Efficiency in x-direction, η_x

Fig. 22 Installation effect on propeller efficiencies η_p and η_x. Experimental results of the clean configuration, $\beta = 0$ deg.

A more interesting quantity from an aircraft performance perspective is the propeller efficiency in the direction of flight, η_x, as it directly affects the fuel consumption for a given flight condition. Typically, for an isolated propeller, η_x decreases with angle of attack because the normal force has a negative contribution in flight direction that completely offsets the higher efficiency due to the reduced axial inflow. To the contrary, for the installed propeller, η_x increases from $\alpha = 0$ up to $\alpha = 5$ deg, as plotted in Fig. 22b. This increase is caused by the reduced propeller normal force that is minimal at a positive angle of attack due to the propeller operating in the wing-induced flowfield. The second peak around $\alpha = 14$ deg for the outboard-up rotating propeller is in line with the trend of η_p. This means that the outboard-up configuration has a larger range of angle of attack at which η_x is close to the maximum. Therefore, it has the potential of better climb performance from a propulsive efficiency point of view than the inboard-up configuration.

The high-lift condition is important for several design considerations, e.g., the design of wing and high lift devices. A decomposition of the airframe and propeller contributions in these conditions is depicted in Fig. 23. The propeller contribution to lift is approximately linear with α and is the dominating contribution to ΔC_L. The strong wing-induced downwash field causes C_{L_p} to be negative for low to moderate angles of attack. If the propellers were to be mounted to the leading edge of a wing, a larger propeller lift component could be expected due to the wing upwash. The figure also shows that the change in airframe lift does not vary significantly with angle of attack. This is due to the compensating normal force on each side of the tailplane and nacelle (see Fig. 14c). The nonlinear part in the airframe ΔC_L for $\alpha > 6$ deg is the consequence of the added lift on the tailplane on the inboard-up rotating side, as discussed in Sec. V.A. The propeller and airframe in these conditions combined lead to only a moderate increase in $C_{L_{max}}$ by up to 0.05, and this is nearly independent of propeller thrust, contrary to a wing-mounted propeller configuration.

Several previous studies [1,30] concluded that the trim drag associated with the large center of gravity excursion is a major drawback for aircraft with tailplane-mounted propellers. The trim drag for elevator deflections determined in Sec. V.B at cruise/climb conditions is plotted in Fig. 24. The thrust-induced pitching moment for the outboard-up rotating configuration is partially offset by the additional downforce on the horizontal tailplane. This leads to nearly the same trim-drag curve as the propeller-off condition. In contrast, the inboard-up rotation leads to a larger nose-down pitching moment, which needs to be compensated by trim for all lift coefficients. It is noted that the considered moment reference point is rather forward, leading to relatively large values of $C_{D_{trim}}$. The corotating configuration is not the average between the two rotation directions as in particular the magnitude of $\Delta C_{N_{ht}}$ varies with angle of attack, and therefore the required elevator deflection for trim.

The installation of the propellers also affects the integral airframe lift and drag, and propeller lift, leading to a net change in the lift-to-drag ratio. Whereas for a wing-mounted tractor configuration the propellers enhance L/D and maximum lift [42,86,90,92], for the tail-mounted propeller configuration this not evident. Firstly, the tailplane-mounted propeller operates in the wing downwash field, which reduces the lift contribution of the propeller. Secondly, the tailplane with a low lift coefficient does not necessarily feature reduced drag by the propeller installation. Figure 25 depicts the product of the installed lift-to-drag ratio curves with the propeller efficiency in flight direction. Besides the added lift, the airframe drag slightly reduced for $\alpha \leq 2$ deg, due to the swirl recovery by the tailplane (at $\alpha = 0$ and $J = 1.8$ the drag is reduced by 20 drag counts). However, the maximum airframe lift-to-drag ratio for the corotating configuration remains approximately the same as in the propeller-off condition. If the lift of the propeller is included in the aircraft lift coefficient, the total lift-to-drag ratio is slightly higher at higher angles of attack. At these conditions, both the thrust vector and normal force enhance lift. These results show that the propeller–airframe interaction causes an

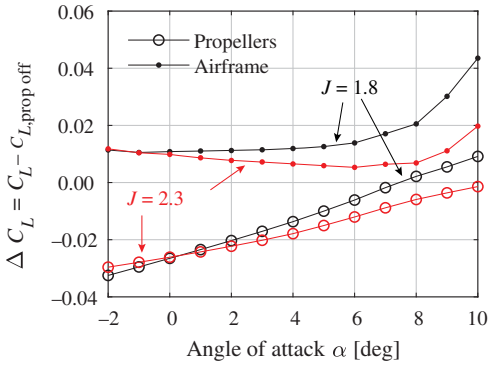

Fig. 23 Change in propeller and airframe lift in installed conditions for the corotating configuration with a flap deflection of $\delta_f = 27$ deg. Experimental results, $\beta = 0$ deg.

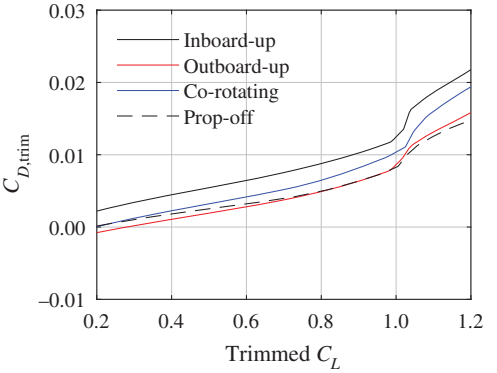

Fig. 24 Trim drag for $C_m = 0$ at $(x,y,z) = (0,0,0)$, clean configuration at $J = 1.6$. Experimental results, $\beta = 0$ deg.

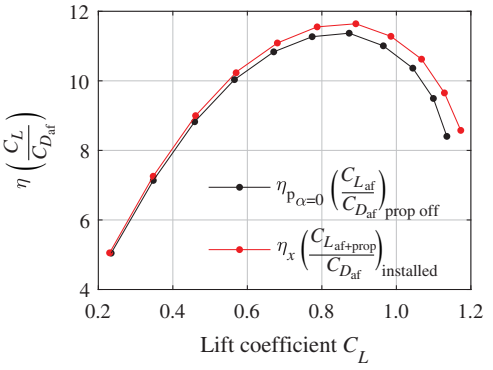

Fig. 25 Propeller installation effect on $\eta(C_L/C_D)$ for the untrimmed corotating configuration at $J = 1.8$. Experimental results of the clean configuration, $\beta = 0$ deg.

appreciable deviation of 2% relative to the performance curve in which the propeller and airframe are treated in isolated conditions.

It is noted that for this particular aircraft the maximum lift-to-drag ratio is at a high value ($C_L = 0.9$), and the magnitude is relatively low because of the suboptimal design of the aircraft. As the benefit discussed in this section in particular is present at higher angles of attack, the benefit would be smaller if the maximum airframe efficiency would be at a lower C_L, e.g., by selecting a different wing incidence angle. The current study displays that even for a suboptimal design, the beneficial propeller–airframe aerodynamic interaction could partially offset the drawbacks identified for the configuration [1,30,90]. These benefits are present despite the fact that an aerodynamic performance benefit historically has not been the objective to study the configuration.

VII. Conclusions

A combined experimental and numerical investigation has been performed using a representative aircraft geometry to characterize the aerodynamic interaction between horizontal tailplane-mounted propellers and the airframe. The rotation direction of the propellers was altered for a range of operating conditions, including variations of angles of attack and sideslip, flap deflection, and elevator deflection. By analyzing the time-averaged propeller–airframe aerodynamic interactions, the changes in aircraft static stability, control, and performance due to the rear-mounted propellers were quantified.

The dominant factor affecting the aircraft pitching moment is the propeller normal force. While the propeller slipstream changes the lift force produced by the horizontal tailplane, this has a much smaller effect on the change in pitching moment. Compared with the normal force of the propeller in isolated conditions, the airframe-induced nonuniform flowfield alters the normal-force curve by a lower gradient and an offset zero angle of attack. This inflow field is primarily induced by the wing as downwash. The propeller normal force gradient is reduced by 17% for the inboard-up and 27% for the outboard-up rotating propeller compared with the isolated propeller. The dependency on rotation direction is primarily caused by the normal force as a consequence of the sidewash toward the symmetry plane that increases with angle of attack. At high angles of attack, the fuselage and separated flow at the wing–fuselage junction cause a significant reduction in effective advance ratio for the outboard-up rotating propeller, leading to a rapid increase in thrust and a large nose-down pitching moment. The propeller normal force gradient in these conditions is three times higher than for an isolated propeller. The propeller contribution to lift is approximately linear with angle of attack and is the dominating contribution to the aircraft lift caused by propeller installation.

The measured flowfield and computed loading distributions show that the outboard-up installation leads to a circulation distribution along the tailplane such that the tailplane-root vortex reduces in strength with angle of attack. This leads to a more effective tailplane for the outboard-up rotating propeller, whereas an inboard-up rotating propeller reduces the tailplane normal force gradient. The neutral point shifts aft with increasing thrust coefficient, up to 5% of the mean aerodynamic chord for a thrust coefficient of $T_C = 0.28$ with corotating propellers. The most forward location of the neutral point is achieved at cruise angles of attack. Only at high angle of attack for which the interaction is dominated by the separated flow from the wing, the change in neutral point becomes negligible for a corotating propeller installation. Therefore, the overall static stability is not adversely affected by the propellers and the propeller-off condition is the critical configuration.

The propeller installation enhances the directional stability by approximately 6–12%, independently of thrust coefficient, where the corotating configuration can be approximated by the side force of two isolated propellers multiplied with their moment arm. The difference between the two rotation directions in case the propellers are located above the fuselage centerline is due a lateral translation of the thrust vector, caused the by the fuselage induced flowfield. In the corotating configuration, a net yawing moment exists that is equivalent to a sideslip angle of 2 deg. This is caused by the thrust-dependent sidewash of the slipstream on the upper side of the horizontal tailplane that initiates from the leading edge of the horizontal tailplane. This sidewash also makes the outboard-up rotating propeller the critical engine for the one-engine-inoperative condition.

It is found that the overall propeller installation requires a positive or negative elevator deflection up to 2 deg in cruise conditions, depending on rotation, to maintain the same moment coefficient as in the propeller-off condition. This rather small input is the result of the thrust-induced nose-down pitching moment, which is largely compensated by the downwash-induced propeller normal force. The outboard-up configuration requires a negligible elevator input, due to the nearly opposite normal force on each side of the tailplane, leading to nearly the same trim-drag curve as the propeller-off condition. In contrast, the inboard-up rotation leads to a larger nose-down pitching moment, which needs to be compensated by trim for all lift coefficients.

The lower propeller normal force at positive angles of attack leads to a higher propeller efficiency in freestream direction compared with an isolated propeller, with a maximum around an angle of attack of 5 deg. The propeller efficiency is further enhanced at high angles of attack for the outboard-up rotating propeller as the wing- and fuselage-induced flowfields lead to a net reduction in the advance ratio for this rotation direction. This makes the propeller efficiency in flight direction multiplied with the lift-to-drag ratio up to 2% higher compared with the situation in which the interaction is not included.

Acknowledgments

The research presented in this paper has been performed in the framework of the Innovative turbopROp configuratioN (IRON) research project and has received funding from the Clean Sky 2 Joint Undertaking under the European Union's Horizon 2020 research and innovation program under Grant Agreement no. 699715. The IRON project is part of the Clean Sky 2 REG-GAM 2018 project implemented on the H2020 program under Grant Agreement no. 807089. The authors are grateful to the partners of the IRON consortium for their contributions and feedback. The authors would like to thank Peter den Dulk and Ed Roessen for the manufacturing of the aircraft model.

References

[1] Goldsmith, I. M., "A Study to Define the Research and Technology Requirements for Advanced Turbo/Propfan Transport Aircraft," NASA CR-166138, 1981.

[2] Miley, S. J., and von Lavante, E., "Propeller Propulsion System Integration—State of Technology Survey," NASA CR-3882, 1985.

[3] Hager, R. D., and Vrabel, D., "Advanced Turboprop Project," NASA SP-495, 1988.

[4] Whitlow, J. B., and Sievers, G. K., "Fuel Savings Potential of the NASA Advanced Turboprop Program," NASA TM-83736, 1984.

[5] Dittmar, J. H., "An Experimental Investigation of Reducing Advanced Turboprop Cabin Noise by Wing Shielding," AIAA Paper 1986-1966, 1986.
https://doi.org/10.2514/6.1986-1966

[6] Revell, J. D., and Tullis, R. H., "Fuel Conservation Merits of Advanced Turboprop Transport Aircraft," NASA CR-152096, 1977.

[7] Khalid, S. A., Lurie, D., Breeze-Stringfellow, A., Wood, T., Ramakrishnan, K., Paliath, U., Wojno, J., Janardan, B., Goerig, T., and Opalski, A., "Open Rotor Engine Aeroacoustic Technology Final Report," Federal Aviation Administration TR DOT/FAA/AEE/2014-04, Washington, D.C., 2012.

[8] Dron, S., "Toward ACARE 2020: Innovative Engine Architectures to Achieve the Environmental Goals?" *26th ICAS Congress*, International Council of the Aeronautical Sciences (ICAS) Paper 2008-4.2.2, Nice, France, 2008.

[9] Lange, R. H., "Review of Advanced Turboprop Transport," *Progress in Aerospace Sciences*, Vol. 23, No. 2, 1986, pp. 151–166. https://doi.org/10.1016/0376-0421(86)90003-5

[10] Epstein, A. H., "Aeropropulsion for Commercial Aviation in the Twenty-First Century and Research Directions Needed," *AIAA Journal*, Vol. 52, No. 5, 2014, pp. 901–911. https://doi.org/10.2514/1.J052713

[11] Van Zante, D., Collier, F., Orton, A., Khalid, S., Wojno, J., and Wood, T., "Progress in Open Rotor Propulsors: The FAA/GE/NASA Open Rotor Test Campaign," *Aeronautical Journal*, Vol. 118, No. 1208, 2014, pp. 1181–1213. https://doi.org/10.1017/S0001924000009842

[12] Dugan, J. F., Jr., Gatzen, B. S., and Adamson, W. M., "Prop-Fan Propulsion–Its Status and Potential," Soc. of Automotive Engineers TP 780995, Warrendale, PA, 1978. https://doi.org/10.4271/780995

[13] Jackson, A. H., Jr., and Gatzen, B. S., "Multi-Mission Uses for Prop-Fan Propulsion," *AGARD Conference Proceedings*, AGARD CP-205, 1976.

[14] Guynn, M. D., Berton, J. J., Haller, W. J., Hendricks, E. S., and Tong, M. T., "Performance and Environmental Assessment of an Advanced Aircraft with Open Rotor Propulsion," NASA TM-2012-217772, 2012.

[15] Mikkelson, D. C., Mitchell, G. A., and Bober, L. J., "Summary of Recent NASA Propeller Research," *AGARD Conference Proceedings*, AGARD CP-366, 1984.

[16] Mitchell, G. A., and Mikkelson, D. C., "Summary and Recent Results from the NASA Advanced High-Speed Propeller Research Program," NASA TM-82891, 1982.

[17] Chirico, G., Barakos, G. N., and Bown, N., "Propeller Installation Effects on Turboprop Aircraft Acoustics," *Journal of Sound and Vibration*, Vol. 424, June 2018, pp. 238–262. https://doi.org/10.1016/j.jsv.2018.03.003

[18] Brooks, B. M., and Metzger, F. B., "Acoustic Test and Analysis of Three Advanced Turboprop Models," NASA CR-159667, 1980.

[19] Magliozzi, B., "Advanced Turboprop Noise: A Historical Review," AIAA Paper 1984-2261, 1984. https://doi.org/10.2514/6.1984-2261

[20] Unruh, J. F., "Installation Effects on Propeller Wake/Vortex-Induced Structure-Borne Noise Transmissions," *Journal of Aircraft*, Vol. 27, No. 5, 1990, pp. 444–448. https://doi.org/10.2514/3.25296

[21] Loeffler, I. J., "Structureborne Noise Control in Advanced Turboprop Aircraft," AIAA Paper 1987-530, 1987. https://doi.org/10.2514/6.1987-530

[22] Salikuddin, M., Tanna, H. K., Burrin, R. H., and Carter, W. E., "Application of Active Noise Control to Model Propeller Noise," *AGARD Conference Proceedings*, AGARD CP-366, 1984.

[23] Revell, J. D., Balena, F. J., and Koval, L. R., "Analysis of Interior Noise-Control Treatments for High-Speed Propeller-Driven Aircraft," *Journal of Aircraft*, Vol. 19, No. 1, 1982, pp. 31–38. https://doi.org/10.2514/3.57352

[24] SenGupta, G., "Reduction of Cabin Noise During Cruise Conditions by Stringer and Frame Damping," *AIAA Journal*, Vol. 17, No. 3, 1979, pp. 229–236. https://doi.org/10.2514/3.61106

[25] Metzger, F. B., "The State of the Art in Prop-Fan and Turboprop Noise," *AGARD Conference Proceedings*, AGARD CP-366, 1984.

[26] Metzger, F. B., "Measurements and Predictions of Turboprop Noise at High Cruise Speed," AIAA Paper 1983-689, 1983. https://doi.org/10.2514/6.1983-689

[27] Succi, G. P., "Design of Quiet Efficient Propellers," Society of Automobile Engineers, Technical Paper 790584, 1979. https://doi.org/10.4271/790584

[28] Jeracki, R., Mikkelson, D., and Blaha, B., "Wind Tunnel Performance of Four Energy Efficient Propellers Designed for Mach 0.8 Cruise," Soc. of Automotive Engineers TP 790573, Warrendale, PA, 1979. https://doi.org/10.4271/790573

[29] Romeu, J., Ignacio Palacios, J., Balastegui, A., and Pamies, T., "Optimization of the Active Control of Turboprop Cabin Noise," *Journal of Aircraft*, Vol. 52, No. 5, 2015, pp. 1386–1393. https://doi.org/10.2514/1.C032431

[30] "Energy Consumption Characteristics of Transports Using the Prop-Fan Concept," Boeing Preliminary Design Department, NASA CR-137937, 1976.

[31] Guo, Y., and Thomas, R. H., "System Noise Assessment of Hybrid Wing–Body Aircraft with Open-Rotor Propulsion," *Journal of Aircraft*, Vol. 52, No. 6, 2015, pp. 1767–1779. https://doi.org/10.2514/1.C033048

[32] Mixson, J. S., Farassat, F., Leatherwood, J. D., Prydz, R., and Revell, J. D., "Interior Noise Considerations for Advanced High-Speed Turboprop Aircraft," *Journal of Aircraft*, Vol. 20, No. 9, 1983, pp. 791–798. https://doi.org/10.2514/3.44944

[33] Renninson, D. C., Wilby, J. F., Marsh, A. H., and Wilby, E. G., "Interior Noise Control Prediction Study for High-Speed Propeller-Driven Aircraft," NASA CR-159200, 1979.

[34] Hanson, D. B., and Magliozzi, B., "Propagation of Propeller Tone Noise Through a Fuselage Boundary Layer," *Journal of Aircraft*, Vol. 22, No. 1, 1985, pp. 63–70. https://doi.org/10.2514/3.45081

[35] Sinnige, T., Della Corte, B., de Vries, R., Avallone, F., Merino-Martínez, R., Ragni, D., Eitelberg, G., and Veldhuis, L. L. M., "Alleviation of Propeller-Slipstream-Induced Unsteady Pylon Loading by a Flow-Permeable Leading Edge," *Journal of Aircraft*, Vol. 56, No. 3, 2019, pp. 1214–1230. https://doi.org/10.2514/1.C035250

[36] Sullivan, W. E., Turnberg, J. E., and Violette, J. A., "Large-Scale Advanced Prop-Fan Blade Design," NASA CR-174790, 1984.

[37] Nicolosi, F., Corcione, S., Della Vecchia, P., Trifari, V., and Ruocco, M., "Aerodynamic Design and Analysis of an Innovative Regional Turboprop Configuration," *31st ICAS Congress*, International Council of the Aeronautical Sciences (ICAS) Paper 2018-0191, Belo Horizonte, Brazil, 2018.

[38] Boctor, M. L., Clay, C. W., and Watson, C. F., "An Analysis of Prop-Fan Airframe Aerodynamic Integration," NASA CR 152186, 1978.

[39] Hirano, H., and Trapp, L. G., "Airframe-Integrated Propeller-Driven Propulsion Systems," U.S. Patent US2016/0244150 A1, Aug. 2016.

[40] Draper, J. W., and Kuhn, R. E., "Investigation of the Aerodynamic Characteristics of a Model Wing-Propeller Combination and of the Wing and Propeller Separately at Angles of Attack up to 90 Degrees," NACA TN 3304, 1954.

[41] van Arnhem, N., Sinnige, T., Stokkermans, T. C. A., Eitelberg, G., and Veldhuis, L. L. M., "Aerodynamic Interaction Effects of Tip-Mounted Propellers Installed on the Horizontal Tailplane," AIAA Paper 2018-0542, 2018. https://doi.org/10.2514/6.2018-0542

[42] Sinnige, T., van Arnhem, N., Stokkermans, T. C. A., Eitelberg, G., and Veldhuis, L. L. M., "Wingtip-Mounted Propellers: Aerodynamic Analysis of Interaction Effects and Comparison with Conventional Layout," *Journal of Aircraft*, Vol. 56, No. 1, 2018, pp. 295–312. https://doi.org/10.2514/1.C034978

[43] Perkins, C. D., and Hage, R. E., *Airplane Performance, Stability and Control*, Wiley, New York, 1949, pp. 231–242, Sec. 5.6.

[44] Phillips, W. F., Anderson, E. A., and Kelly, Q. J., "Predicting the Contribution of Running Propellers to Aircraft Stability Derivatives," *Journal of Aircraft*, Vol. 40, No. 6, 2003, pp. 1107–1114. https://doi.org/10.2514/2.7221

[45] Obert, E., "A Method for the Determination of the Effect of Propeller Slipstream on the Static Longitudinal Stability and Control of Multi-Engined Aircraft," Delft Univ. of Technology TR LR-761, Delft, The Netherlands, 1994.

[46] van der Vaart, J. C., and Muhammad, H., "Static Longitudinal Stability and Control Characteristics of the Fokker F27 'Friendship' Calculated by Simple Handbook Methods," Delft Univ. of Technology TR LR-394, Delft, The Netherlands, 1983.

[47] Eshelby, M. E., "On the Aerodynamics of Installed Propellers," *AGARD Conference Proceedings*, AGARD CP-366, 1984.

[48] Qin, E., Yang, G., and Li, F., "Numerical Analysis of the Interference Effect of Propeller Slipstream on Aircraft Flowfield," *Journal of Aircraft*, Vol. 35, No. 1, 1998, pp. 84–90. https://doi.org/10.2514/2.2263

[49] Keller, D., and Rudnik, R., "Numerical Investigation of Engine Effects on a Transport Aircraft with Circulation Control," *Journal of Aircraft*, Vol. 52, No. 2, 2015, pp. 421–438. https://doi.org/10.2514/1.C032724

[50] van Rooyen, R. S., and Eshelby, M. E., "Assessment of Propeller Influence on Lateral-Directional Stability of Multiengine Aircraft,"

Journal of Aircraft, Vol. 18, No. 5, 1981, pp. 364–371. https://doi.org/10.2514/3.44710

[51] Schroijen, M. J. T., Veldhuis, L. L. M., and Slingerland, R., "Propeller Empennage Interaction Effects on Vertical Tail Design of Multiengine Aircraft," *Journal of Aircraft*, Vol. 47, No. 4, 2010, pp. 1133–1140. https://doi.org/10.2514/1.46707

[52] Schroijen, M. J. T., Veldhuis, L. L. M., and Slingerland, R., "Propeller Slipstream Investigation Using the Fokker F27 Wind Tunnel Model with Flaps Deflected," *26th ICAS Conference*, International Council of the Aeronautical Sciences (ICAS) Paper 2008-3.1.2, Anchorage, Alaska, 2008.

[53] Dorsey, A. M., and Uranga, A., "Design Space Exploration of Future Open Rotor Configurations," AIAA Paper 2020-3680, 2020. https://doi.org/10.2514/6.2020-3680

[54] Nicolosi, F., Corcione, S., Trifari, V., Cusati, V., Ruocco, R., and Della Vecchia, P., "Performance Evaluation and DOC Estimation of an Innovative Turboprop Configuration," AIAA Paper 2018-3662, 2018. https://doi.org/10.2514/6.2018-3662

[55] Nicolosi, F., Corcione, S., Trifari, V., Della Vecchia, P., and De Marco, A., "Design Guidelines for High Capacity Innovative Regional Turboprop Aircraft," *AIAA Scitech*, AIAA Paper 2019-02561, 2019. https://doi.org/10.2514/6.2019-02561

[56] Vos, R., and Hoogreef, M., "System-Level Assessment of Tail-Mounted Propellers for Regional Aircraft," *31st Congress of the International Council of the Aeronautical Sciences*, ICAS Paper 2018-0065, Belo Horizonte, Brazil, 2018.

[57] Kroo, I., "Propeller/Wing Integration for Minimum Induced Loss," *Journal of Aircraft*, Vol. 23, No. 7, 1986, pp. 561–565. https://doi.org/10.2514/3.45344

[58] Cole, J. A., Krebs, T., Barcelos, D., and Bramesfeld, G., "Influence of Propeller Location, Diameter, and Rotation Direction on Aerodynamic Efficiency," *Journal of Aircraft*, Vol. 58, No. 1, 2020, pp. 63–71. https://doi.org/10.2514/1.C035917

[59] Snyder, M. H., Jr., and Zumwalt, G. W., "Effects of Wingtip-Mounted Propellers on Wing Lift and Induced Drag," *Journal of Aircraft*, Vol. 6, No. 5, 1969, pp. 392–397. https://doi.org/10.2514/3.44076

[60] Coe, P., Jr., Applin, Z., and Williams, L., "Stability and Control Results for Advanced Turboprop Aft-Mount Installations," Soc. of Automotive Engineers TP 841479, Warrendale, PA, 1984. https://doi.org/10.4271/841479

[61] Dunham, D. M., Gentry, G. L., Jr., Manuel, G. S., Applin, Z. T., and Quinto, P. F., "Low-Speed Aerodynamic Characteristics of a Twin-Engine General Aviation Configuration with Aft-Fuselage-Mounted Pusher Propellers," NASA TP 2763, 1987.

[62] Ridder, S. O., "Wind Tunnel of a Twin, Rear Propeller Transport Aircraft Configuration at Low Speeds," *14th ICAS Congress*, International Council of the Aeronautical Sciences (ICAS) Paper 1984-2.6.3, Toulouse, France, 1984.

[63] de Young, J., "Propellers at High Incidence," *Journal of Aircraft*, Vol. 23, No. 3, 1965, pp. 241–250. https://doi.org/10.2514/3.43646

[64] Serpieri, J., "Cross-Flow Instability: Flow Diagnostics and Control of Swept Wing Boundary Layers," Ph.D. Thesis, Delft Univ. of Technology, Delft, The Netherlands, 2018. https://doi.org/10.4233/uuid:3dac1e78-fcc3-437f-9579-048b74439f55

[65] Howe, D., and Rorie, G., *Aircraft Conceptual Design Synthesis*, Professional Engineering Publ., London, 2000, pp. 130–131.

[66] Kundu, A. K., *Aircraft Design*, Vol. 27, Cambridge Univ. Press, Cambridge, England, U.K., 2010, pp. 85–86.

[67] Raymer, D., *Aircraft Design: A Conceptual Approach*, AIAA, Reston, VA, 1992, p. 51.

[68] Roskam, J., *Airplane Design Part II: Preliminary Configuration Design and Integration of the Propulsion System*, DARcorporation, Lawrence, KS, 2018, pp. 144–145.

[69] Schaufele, R. D., *The Elements of Aircraft Preliminary Design*, Aries Publ., Santa Anna, CA, 2000, p. 101.

[70] Sinnige, T., de Vries, R., Della Corte, B., Avallone, F., Ragni, D., Eitelberg, G., and Veldhuis, L. L. M., "Unsteady Pylon Loading Caused by Propeller-Slipstream Impingement for Tip-Mounted Propellers," *Journal of Aircraft*, Vol. 55, No. 4, 2018, pp. 1605–1618. https://doi.org/10.2514/1.C034696

[71] van Arnhem, N., de Vries, R., Sinnige, T., Vos, R., Eitelberg, G., and Veldhuis, L. L. M., "Engineering Method to Estimate the Blade Loading of Propellers in Nonuniform Flow," *AIAA Journal*, Vol. 58, No. 12, 2020, pp. 5332–5346. https://doi.org/10.2514/1.J059485

[72] de Vries, R., van Arnhem, N., Avallone, F., Ragni, D., Vos, R., Eitelberg, G., and Veldhuis, L. L. M., "Experimental Investigation of Over-the-Wing Propeller–Boundary-Layer Interaction," *AIAA Journal*, Vol. 59, No. 6, 2021, pp. 2169–2182. https://doi.org/10.2514/1.J059770

[73] de Vries, R., van Arnhem, N., Avallone, F., Ragni, D., Vos, R., Eitelberg, G., and Veldhuis, L. L. M., "Aerodynamic Interaction Between Propellers of a Distributed-Propulsion System in Forward Flight," *Aerospace Science and Technology*, Vol. 118, Nov. 2021, Paper 107009. https://doi.org/10.1016/j.ast.2021.107009

[74] Tripp, J. S., and Tcheng, P., "First International Symposium on Strain Gauge Balances," NASA CP-1999-209101/PT2, 1999.

[75] Hufnagel, K., and Quade, M., "The 2nd Generation Balance Calibration Machine of Darmstadt University of Technology," AIAA Paper 2007-148, 2007. https://doi.org/10.2514/6.2007-148

[76] Gracey, W., Letko, W., and Russel, W. R., "Wind-Tunnel Investigation of a Number of Total-Pressure Tubes at High Angles of Attack," NACA TN 2331, 1951.

[77] Stokkermans, T. C. A., van Arnhem, N., Sinnige, T., and Veldhuis, L. L. M., "Validation and Comparison of RANS Propeller Modeling Methods for Tip-Mounted Applications," *AIAA Journal*, Vol. 57, No. 2, 2019, pp. 566–580. https://doi.org/10.2514/1.J057398

[78] "Help System, Fluent," ANSYS® Academic Research Release 18.1, ANSYS, Inc., Canonsburg, PA, 2017.

[79] Spalart, P. R., and Rumsey, C. L., "Effective Inflow Conditions for Turbulence Models in Aerodynamic Calculations," *AIAA Journal*, Vol. 45, No. 10, 2007, pp. 2544–2553. https://doi.org/10.2514/1.29373

[80] Hoerner, S. F., *Interference Drag*, Hoerner Fluid Dynamics, Bakersfield, CA, 1965, Chap. 8.10.

[81] Ruiz-Calavera, L. P., and Perdones-Diaz, D., "CFD Computation of In-Plane Propeller Shaft Loads," AIAA Paper 2013-3798, 2013. https://doi.org/10.2514/6.2013-3798

[82] Peake, D. J., and Tobak, M., "Three-Dimensional Interactions and Vortical Flows with Emphasis on High Speeds," AGARD, AGARD-AG-252, 1980.

[83] Surana, A., Grunberg, O., and Haller, G., "Exact Theory of Three-Dimensional Flow Separation. Part 1. Steady Separation," *Journal of Fluid Mechanics*, Vol. 564, Sept. 2006, pp. 57–103. https://doi.org/10.1017/S0022112006001200

[84] Leweke, T., Le Dizés, S., and Williamson, C. H. K., "Dynamics and Instabilities of Vortex Pairs," *Annual Review of Fluid Mechanics*, Vol. 48, Jan. 2016, pp. 507–541. https://doi.org/10.1146/annurev-fluid-122414-034558

[85] Gand, F., Monnier, J.-C., Deluc, J.-M., and Choffat, A., "Experimental Study of the Corner Flow Separation on a Simplified Junction," *AIAA Journal*, Vol. 53, No. 10, 2015, pp. 2869–2877. https://doi.org/10.2514/1.J053771

[86] Veldhuis, L. L. M., "Propeller Wing Aerodynamic Interference," Ph.D. Thesis, Delft Univ. of Technology, Delft, The Netherlands, 2005.

[87] Applin, Z. T., and Coe, P. L., Jr., "Low-Speed Stability and Control Characteristics of a Transport Model with Aft-Fuselage-Mounted Advanced Turboprops," NASA TR NT-2535, 1986.

[88] Felli, M., "Underlying Mechanisms of Propeller Wake Interaction with a Wing," *Journal of Fluid Mechanics*, Vol. 908, Dec. 2020, Paper A10. https://doi.org/10.1017/jfm.2020.792

[89] Wolowicz, C. H., and Yancey, R. B., "Lateral-Directional Aerodynamic Characteristics of Light, Twin-Engine, Propeller-Driven Airplanes," NASA TN-6946, 1972.

[90] Mann, S. A. E., and Stuart, C. A., "Advanced Propulsion Through the 1990s, An Airframers View," AIAA Paper 1985-1192, 1985. https://doi.org/10.2514/6.1985-1192

[91] Küchemann, D., and Weber, J., "5–An Analysis of Some Performance Aspects of Various Types of Aircraft Designed to Fly over Different Ranges at Different Speeds," *Progress in Aeronautical Sciences*, Vol. 9, 1968, pp. 329–456. https://doi.org/10.1016/B978-1-4831-9985-6.50008-4

[92] Muehlbauer, J. C., Hewell, J. G., Jr., Lindenbaum, S. P., Randall, C. C., Searle, N., and Stone, F. R., Jr., "Turboprop Cargo Aircraft Systems Study Phase 1," NASA TR NAS 1-15708, 1980.

This article has been cited by:

1. Reynard de Vries, Nando van Arnhem, Tomas Sinnige, Roelof Vos, Leo L.M. Veldhuis. 2021. Aerodynamic interaction between propellers of a distributed-propulsion system in forward flight. *Aerospace Science and Technology* **118**, 107009. [Crossref]